TU Delft

Delft University of Technology

Size-dependent strength superiority in multi-principal element alloys versus constituent metals

Insights from machine-learning atomistic simulations

Shuang, Fei; Ji, Yucheng; Laurenti, Luca; Dey, Poulumi

DOI
10.1016/j.ijplas.2025.104308

Licence
CC BY

Publication date
2025

Document Version
Final published version

Published in
International Journal of Plasticity

Citation (APA)
Shuang, F., Ji, Y., Laurenti, L., & Dey, P. (2025). Size-dependent strength superiority in multi-principal element alloys versus constituent metals: Insights from machine-learning atomistic simulations. *International Journal of Plasticity*, *188*, Article 104308. https://doi.org/10.1016/j.ijplas.2025.104308

Important note
To cite this publication, please use the final published version (if applicable).
Please check the document version above.

Copyright
Other than for strictly personal use, it is not permitted to download, forward or distribute the text or part of it, without the consent of the author(s) and/or copyright holder(s), unless the work is under an open content license such as Creative Commons.

Takedown policy
Please contact us and provide details if you believe this document breaches copyrights.
We will remove access to the work immediately and investigate your claim.

This work is downloaded from Delft University of Technology.
For technical reasons the number of authors shown on this cover page is limited to a maximum of 10.

International Journal of Plasticity 188 (2025) 104308

Contents lists available at ScienceDirect

International Journal of Plasticity

journal homepage: www.elsevier.com/locate/ijplas

Size-dependent strength superiority in multi-principal element alloys versus constituent metals: Insights from machine-learning atomistic simulations

Fei Shuang [a,*], Yucheng Ji [a,b], Luca Laurenti [c], Poulumi Dey [a,*]

[a] Department of Materials Science and Engineering, Faculty of Mechanical Engineering, Delft University of Technology, Mekelweg 2, Delft 2628 CD, the Netherlands

[b] Beijing Advanced Innovation Center for Materials Genome Engineering, National Materials Corrosion and Protection Data Center, Institute for Advanced Materials and Technology, University of Science and Technology Beijing, Beijing 100083, China

[c] Delft Centre of System and Control, Faculty of Mechanical Engineering, Delft University of Technology, Mekelweg 2, Delft 2628 CD, the Netherlands

ARTICLE INFO

Keywords:
Multi-principal element alloy
MoNbTaW
Machine learning interatomic potential
Plastic mechanism
Size effect

ABSTRACT

Multi-principal element alloys (MPEAs) are renowned for their enhanced mechanical strength relative to their constituent metals, as evidenced by various experimental techniques such as tension/compression tests and instrumental indentation. Nevertheless, atomistic simulations sometimes produce conflicting results, casting doubt on the consistently superior mechanical properties of MPEAs. In this study, machine-learning interatomic potentials (MLIPs) with first-principles accuracy were developed for body-centered cubic refractory MoNbTaW MPEAs, enabling systematic atomistic simulations under various deformation scenarios. The new MLIPs are supported by a comprehensive dataset encompassing extensive defects, and the established embedded-atom model (EAM) potential was benchmarked against both this dataset and the new MLIP. Simulations covering diverse compositions confirm that both MLIPs and EAM accurately capture the critical strengthening mechanisms in MoNbTaW MPEAs. It is revealed that MPEAs generally exhibit superior mechanical strength compared to their constituent metals in macro-scale specimens, primarily due to solid solution strengthening during dislocation motion. However, at the nanoscale—where plasticity is predominantly governed by dislocation nucleation and grain boundary deformation—the constituent metals may outperform MPEAs. A critical length scale is identified above which MPEAs demonstrate enhanced mechanical strength relative to their constituent elements; below this scale, the advantage diminishes, underscoring a significant size-dependent effect that is crucial for optimizing MPEA applications, particularly at the nanoscale.

1. Introduction

Multi-Principal Element Alloys (MPEAs), which encompass high-entropy alloys (HEAs) and medium-entropy alloys (MEAs), represent a significant departure from conventional metals and alloys (George et al., 2019; Miracle and Senkov, 2017). They are characterized by four core effects: the high-entropy effect, severe lattice distortion, sluggish diffusion, and the cocktail effect (Hsu

* Corresponding authors.
E-mail addresses: F.Shuang@tudelft.nl (F. Shuang), P.dey@tudelft.nl (P. Dey).

https://doi.org/10.1016/j.ijplas.2025.104308
Received 25 November 2024; Received in revised form 12 March 2025;
Available online 16 March 2025
0749-6419/© 2025 The Authors. Published by Elsevier Ltd. This is an open access article under the CC BY license (http://creativecommons.org/licenses/by/4.0/).

et al., 2024). These distinctive effects imbue MPEAs with unique properties that have captured the interest of researchers across various disciplines (Wang et al., 2024a). For example, they are used as strong and ductile structural materials capable of performing under extreme cryogenic conditions (Bai et al., 2023; Gludovatz et al., 2014), even at temperatures as low as 20 K (Liu et al., 2022). MPEAs show exceptional impact toughness (Li and Zhang, 2016) and fatigue resistance (Zhu et al., 2024). MPEAs also show promise in mitigating hydrogen embrittlement (Luo et al., 2020, 2018; Tan et al., 2024). Furthermore, their exceptional radiation resistance makes them indispensable in the development of nuclear fusion energy systems (El-Atwani et al., 2019; Granberg et al., 2016; Lu et al., 2016). Additionally, MPEAs are critical in advancing hydrogen storage and production technologies (Ma et al., 2021) and enhancing catalytic processes (Sun and Dai, 2021), thereby contributing to the advancement of sustainable energy solutions.

One of the most intriguing features of MPEAs is their remarkable mechanical strength compared to their constituent elements, which can be mostly attributed to solid solution strengthening due to lattice distortion-induced roughed energy landscape (George et al., 2020; Lee et al., 2021; Varvenne et al., 2016a). Experimental evidence strongly supports this observation. For face-centered cubic (FCC)-type MPEAs, it was found experimentally that the Cantor alloy (FeMnCrCoNi) and its subsystems display higher strength than Ni (Wu et al., 2014b). Furthermore, CrCoNi was found to exhibit superior tensile properties compared to the Cantor alloy (Laplanche et al., 2017). Subsequent experiments revealed that CrFeCoNiPd (Ding et al., 2019) and VCoNi (Su Sohn et al., 2019) show even higher strength than CrCoNi. These experiments typically utilized dog-bone-shaped specimens to measure the bulk strength. Additionally, other experiments demonstrated that the Vickers hardness of FeNiCrCo alloys is significantly higher than that of pure Ni (Wu et al., 2014a). For body-centered cubic (BCC) MPEAs, similarly, experiments found that $Mo_{25}Nb_{25}Ta_{25}W_{25}$ and $Mo_{20}Nb_{20}Ta_{20}W_{20}V_{20}$ exhibit higher hardness than their constituent elements (Senkov et al., 2010; Zou et al., 2014). Moreover, systematic mechanical tests on nanopillars with different sizes showed that $Mo_{25}Nb_{25}Ta_{25}W_{25}$ exhibit higher compressive strength than constituent elements (Zou et al., 2014). Yet, these findings may contribute to a widespread misconception in current research that MPEAs invariably outperform constituent metals in terms of strength.

Additionally, atomistic simulations plays a significant role in studying the deformation mechanisms of MPEAs and pure metals under various loading conditions (Dai et al., 2022; Gupta et al., 2022; Ji et al., 2020; Jian et al., 2022; Li et al., 2024; Romero et al., 2022; Xie et al., 2022; Xiong et al., 2015; Zhang et al., 2023b). The emergence of machine learning interatomic potentials (MLIPs) has made atomistic simulations even more attractive and promising, as they can approach density functional theory (DFT) accuracy (Poul et al., 2023; Santos-Florez et al., 2023; Xu et al., 2024; Yin et al., 2021). One of the most common applications of atomistic simulations is investigating the solid solution strengthening in MPEAs using simple shear loading in the periodic array of dislocation (PAD) model (Yin et al., 2021). These simulations were also employed to study dislocation mobility and the effects of chemical short-range ordering (CSRO) (Huang et al., 2024). Under this simple loading condition, the strength of MPEAs is significantly higher than that of constituent metals, which is consistent with theoretical predictions from the solid solution strengthening models (Maresca and Curtin, 2020a; Varvenne et al., 2016a) and experimental observations (Baruffi et al., 2022; George et al., 2020). Moreover, numerous atomistic simulation studies have simulated different deformation mechanisms under different loading conditions. Since a large number of atoms were used in these studies, embedded-atom method (EAM) or modified embedded-atom method (MEAM) potentials were usually adopted (Cao, 2022; Jian et al., 2020). Among the numerous computational studies of MPEAs, only a few works compare the mechanical strength of MPEAs with that of their constituent metals. For instance, the hardness of BCC HfNbTaTiZr, both with and without SRO, was found to be significantly lower than that of pure BCC Ta (Alhafez et al., 2024). The hardness of FCC FeMnCrCoNi was revealed to be lower than that of pure Ni (Alabd Alhafez et al., 2019). Another study indicated that with a twin boundary inside, pure Ni exhibits higher hardness than FeMnCrCoNi (Shuang et al., 2021). The hardness of CrCoNi was subsequently found to be slightly lower than Ni (Hua et al., 2021). Additionally, a systematic virtual tensile simulations of columnar polycrystalline samples showed that both Ni and Cr exhibit higher strength at 5% deformation than FeNiCrCoCu (Farkas, 2021). Moreover, in the tensile simulations of single crystalline Ni and FeMnCrCoNi alloy and its subsystems, the MEAM potential-based results showed that FeMnCrCoNi exhibit lower strength than pure Ni (Choi et al., 2018). Another large-scale tensile simulation of CrCoNi, CoCrFeNi and Al0.1CoCrFeNi revealed their lower strength than pure Ni, with these MPEAs exhibiting larger elongation before failure than pure Ni (Zhang et al., 2023a). For BCC MPEAs, nanopillar compression simulations of AlCoCrCu0.5FeNi showed significantly lower stress than the pure BCC Fe using EAM potential (Li et al., 2019b). Additionally, the MLIP-based simulations revealed that W exhibits the higher flow stress than $Mo_{25}Nb_{25}Ta_{25}W_{25}$ in polycrystal compression simulations (Li et al., 2020).

As evident from the above discussion, it is observed that the experimental results contradict the findings of atomistic simulations. While experiments typically indicate higher strength for MPEAs compared to constituent metals, simulations show the opposite. The observed contradiction between prior experiments and simulations suggests the existence of a critical length scale. This length scale demarcates the regime where MPEAs exhibit superior strength compared to constituent metals above this scale, whereas pure metals outperform MPEAs below it. This intriguing hypothesis forms the basis of our study. To test this hypothesis and explore the underlying mechanisms, one can either perform nanoscale strength measurements of MPEAs and their constituent metals experimentally, or conduct detailed atomistic simulations. Given the emphasis on computational methods, the investigation focuses exclusively on simulations in this study. However, a significant challenge persists: the prevalent EAM potentials are overly simplistic for MPEAs, and existing MLIPs do not accurately simulate complex plastic deformation, as they often exclude defects during their training processes.

In this study, new MLIPs were developed specifically for modeling complex plasticity in BCC MoNbTaW MPEAs by integrating extensive defects into the training process. The established EAM-Zhou potential was benchmarked using DFT datasets generated in this study, alongside the newly developed MLIPs. Furthermore, systematic atomistic simulations were performed regarding edge dislocation motion, GB deformation and dislocation nucleation in different compositions with high fidelity. This enables an assessment of the strength superiority of MPEAs compared to their constituent metals under various deformation scenarios. Finally, an atypical size effect was investigated in MPEAs using mechanistic strength models, highlighting the size-dependent superiority of mechanical

strength across different scales in MPEAs and their constituent metals.

2. Methods

2.1. First principles calculations

The Vienna Ab initio Simulation Package (VASP) (Kresse and Furthmüller, 1996) was utilized to perform DFT calculations of all new configurations necessary for MLIP development. A gradient-corrected functional in the Perdew-Burke-Ernzerhof (PBE) form is used to describe the exchange and correlation interactions (Perdew et al., 1996). Electron-ion interactions are treated within the projector-augmented-wave (PAW) method (Blöchl, 1994), using the standard PAW pseudopotentials provided by VASP. The energy convergence criterion is set to 10^{-6} eV for electronic self-consistency calculations. The plane-wave cutoff energy is chosen to be 520 eV for all systems. The KPOINTS are generated by VASPKIT (Wang et al., 2021), based on the Monkhorst-Pack scheme, with a consistent density of $2\pi \times 0.03$ Å^{-1} across the entire dataset.

2.2. Machine learning potential development

The MLIP-2 package (Novikov et al., 2021) was employed to develop moment tensor potentials (MTPs) for the MoNbTaW systems. MLIP-2 utilizes moment tensor descriptors and applies linear regression to train the machine learning model, enabling it to predict the energy, force, and stress of atomistic systems. MTP is one of the most popular machine learning potentials due to its high accuracy and efficiency (Zuo et al., 2020). Within our study, the weights of energy, force and stress are set as 1, 0.01 and 0, respectively. It should be noted that MTPs have been recently developed for MoNbTaW (MTP14-Yin) (Yin et al., 2021) and MoNbTaWV (MTP-Wang) (Wang et al., 2024c) systems; however, these MTPs do not incorporate defects, such as dislocations, vacancies, and grain boundaries (GBs). Consequently, their accuracy in simulations of general plastic deformation remains unknown.

Two MLIPs, MTP-14-new and MTP-16-new were developed, where the numbers "14" and "16" represent the maximum level of MTP, governing the completeness of the basis functions. The standard template provided by the developers of the MLIP-2 package (Novikov et al., 2021) was employed for the training. As such, the optimization of the radial basis is not considered. Detailed descriptions of the moment tensor descriptors can be found in Ref. Shapeev (2016). During the training process, the energy and force data are assigned weights of 1 and 0.01, respectively, consistent with previous studies (Yin et al., 2021). The weight values are not optimized, as the default values have proven robust across different datasets and have been widely used for MTP training in prior studies (Lee et al., 2023; Sheriff et al., 2024; Zhou et al., 2022; Zuo et al., 2020). Nevertheless, as demonstrated in the following sections, the energy and force errors in both the training and test datasets are exceptionally low, highlighting the effectiveness of our chosen training parameters.

The active learning approach was used to develop an MTP capable of accurately modeling the plastic deformation of single crystals, both with and without vacancies (Novikov et al., 2021). This method utilizes an extrapolation grade (γ), which quantifies the deviation of a given configuration from those in the training set, enabling the estimation of prediction errors without requiring DFT calculations. The process starts by training an MTP on an initial dataset. This MTP is then used to simulate the target system under relevant conditions, reflecting the intended applications. If the simulation encounters structures with γ values exceeding the break threshold ($\gamma_{\text{break}} = 10$), the simulation is stopped. Structures with γ values above the select threshold ($\gamma_{\text{select}} = 2$) are added to the training set, and a new MTP is generated. Notably, these γ thresholds follow the guidelines of Novikov et al. (2021): typically, $\gamma \leq 1$ indicates interpolation, $1 < \gamma \leq 2$ indicates accurate extrapolation, $2 < \gamma \leq 10$ indicates reliable extrapolation, and $\gamma > 10$ indicates risky extrapolation. This iterative cycle continues until the MTP can successfully complete simulations without generating structures with γ exceeding γ_{break}.

Additionally, the extrapolation grade (γ_{atom}), based on the D-optimality criterion (MaxVol algorithm), was used to perform uncertainty quantification for each atom. This approach has been successfully implemented in various MLIP frameworks, including MTP (Podryabinkin et al., 2023) and atomic cluster expansion (ACE) potential (Lysogorskiy et al., 2023). It should be noted that γ_{atom} represents the extrapolation grade for each individual atom, whereas the previously mentioned γ refers to the extrapolation grade for an entire configuration.

2.3. Other interatomic potentials

Apart from MTPs, the extensive DFT datasets were used to evaluate the accuracy of other potentials, including MTP14-Yin (Yin et al., 2021), EAM (Zhou et al., 2004), TabGAP (Byggmästar et al., 2021), MACE (Batatia et al., 2023), and CHGNET (Batatia et al., 2023) for MoNbTaW systems. EAM is based on Zhou's potential (Zhou et al., 2004) and generated by the Python tool from LAMMPS (Thompson et al., 2022). TabGAP is a more comprehensive machine learning potential that includes the additional element V, developed specifically for studying radiation damage in MoNbTaVW systems (Byggmästar et al., 2021). Since MTP14-Yin (Yin et al., 2021), SNAP (Li et al., 2020) and MTP-Wang (Wang et al., 2024c) were trained by the same dataset, we only consider MTP14-Yin in our study. Finally, the accuracy of two recent universal MLIPs (uMLIPs) across the period table: MACE (mace_mp_0) (Batatia et al., 2023) and CHGNET (0.3.0) (Deng et al., 2023), were assessed. It should be noted that uMLIPs are considerably slower than customized MLIPs, with prediction errors around 26~29 meV/atom for the training/validation/test datasets (Deng et al., 2023).

2.4. Atomistic simulations

The Large-scale Atomic/Molecular Massively Parallel Simulator (LAMMPS) package was employed for all atomistic simulations (Thompson et al., 2022). The newly developed MTPs and the existing EAM potential (EAM-Zhou) (Zhou et al., 2004) will be used to describe the interatomic interactions among all elements in MoNbTaW. The average-atom (A-atom) (Varvenne et al., 2016b) interatomic potential will be used for the same system but without lattice distortion. For visualizing atomic configurations and post-processing results such as extracting dislocation lines, we use OVITO (Stukowski, 2010). Additionally, Atomsk is used to generate edge dislocation in the PAD model and polycrystalline structures (Hirel, 2015). These packages provide a comprehensive suite of tools to support our study of the mechanical properties and plastic deformation mechanisms of MPEAs and pure metals.

3. Machine learning potential development with extensive defects

New single-point DFT calculations were carried out on existing 5955 configurations obtained from Ref. Li et al. (2020) using a consistent k-point density. This dataset encompasses undistorted ground state structures, distorted structures subject to differing elastic strains, surface configurations, and snapshots from ab-initio MD simulations for Mo, Nb, Ta, and W. It also includes compositions in the form A_xB_{1-x}, with x varying from 0 to 100 atomic percent at intervals of 6.25%, across all binary systems. Additionally, ab-initio MD snapshots of special quasi-random structures (SQSs) are employed for equimolar ternary and quaternary systems. To enhance the transferability of MTPs for investigating complex plastic deformations, this dataset was expanded to include additional configurations that feature various defects, as illustrated in Fig. 1. The datasets of unstable stacking fault (USF) (Fig. 1(a)), edge dislocation (Fig. 1(b)), and screw dislocation (Fig. 1(c)), totaling 8233 configurations, were combined with the exiting dataset. The configurations were then randomly divide using a 90/10 split for training and testing to develop a new MTP, designated MTP14-new. Additionally, four types of grain boundaries (GBs) (Fig. 1(d)) and vacancies (Fig. 1(e)) were incorporated. For these defects, both pure elements and alloys with varied compositions are considered. Finally, the on-the-fly active learning (AL) technique was employed to simulate the tension and compression of a single crystal of $Mo_{25}Nb_{25}Ta_{25}W_{25}$ in an NPT (isothermal-isobaric) ensemble (AL-NPT-T/C), both with and without a monovacancy (Fig. 1(f)). The inclusion of a monovacancy is employed to generate configurations that exhibit vacancy-induced plasticity. This process captures the phase transition from BCC to FCC and deformation twinning. All new configurations generated in the AL-NPT-T/C simulations are extracted and combined with existing configurations, USF, dislocations,

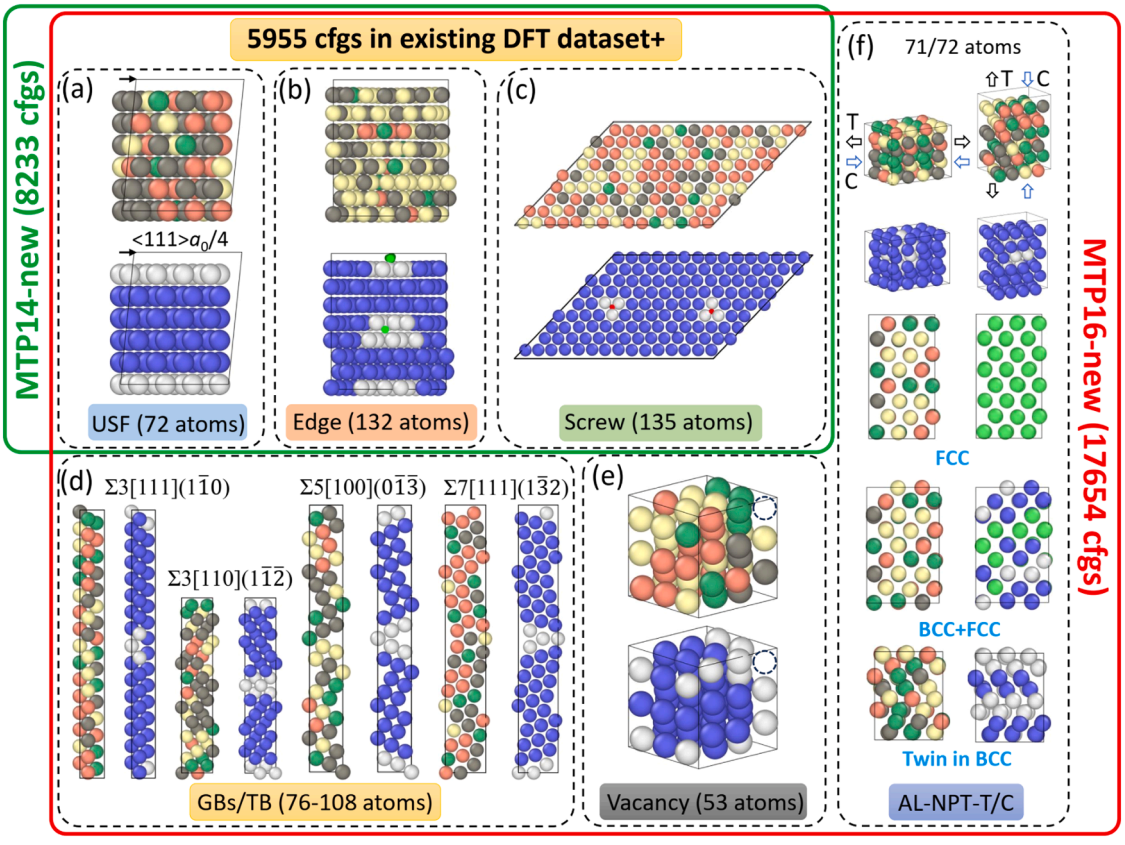

Fig. 1. All configurations used for new MLIPs development. 5955 existing configurations from Ref (Li et al., 2020) and newly added (a) USF, (b) edge and (c) screw datasets are used for training MTP14-new. Additional datasets (d) GBs/TB, (e) vacancy and (f) AL-NPT-NC for MTP-16-new.

vacancy, and GB configurations to construct the complete model. A random split of 90/10 of 17,654 configurations is utilized for the training and testing of a comprehensive MTP model, MTP16-new.

Fig. 2 showcases the performance of the two new MTPs: MTP14-new and MTP16-new. Notably, MTP14-new displays training and test mean absolute errors (MAE) for energy of 3.94/3.95 meV/atom, for force of 42.98/42.72 meV/Å, and for stress of 0.21/0.20 GPa. These values represent a significant improvement in accuracy over previous MLIPs for the same systems, such as SNAP (Li et al., 2020), MTP14-Yin (Yin et al., 2021), and neural network potential (NNP) (Santos-Florez et al., 2023), likely due to consistent k-point density in our DFT calculations. Conversely, MTP16-new exhibits slightly higher energy and force errors (4.44/4.42 meV/atom and 45.28/45.52 meV/Å, respectively) due to the complex defect configurations, but lower stress errors (0.18/0.19 GPa). We highlight that the two MTPs are developed for distinct purposes: MTP14-new is fast so it is intended for simulating edge dislocation strengthening, which requires a large number of atoms due to the dislocation length-dependent strength (Xu et al., 2022). MTP16-new, on the other hand, is designed for simulating complex plastic deformations in polycrystal. It should be noted that although stress is not considered in our training process, the obtained MPTs are still accurate in stress predictions (Fig. 2(c, f)) as compared to NNP (Santos-Florez et al., 2023).

To compare the new MTPs with the existing interatomic potentials, the atomic potential energies were predicted for configurations across all datasets using the potentials discussed in Section 2.3. The MAE of these potentials is summarized in Fig. 3(a). Interestingly, MTP14-Yin, the most widely used potential for MoNbTaW MPEAs, demonstrates high accuracy not only in the existing dataset but also in screw dislocation and TB, despite these configurations not being included in its training process. This suggests that the local atomic environments in these datasets are similar to those in the existing dataset. However, MTP14-Yin's performance is less satisfactory for USF, edge dislocation, vacancy, GB and Al-NPT-T/C, indicating its limitations in simulating complex plastic deformation. As an enhanced iteration of MTP14-Yin, MTP14-new demonstrates significantly improved accuracy on the existing dataset as well as specialized datasets for screw/edge dislocation, and USF, making it well-suited for dislocation simulations. In contrast, MTP16-new exhibits superior accuracy across all datasets, particularly for screw dislocation, vacancy and GB. This broader accuracy range establishes MTP16-new as a comprehensive MLIP for diverse simulation applications. Meanwhile, TabGAP exhibits medium accuracy with an MAE ranging from 13.3 to 26.1 meV/atom. CHGNET and MACE show comparable MAEs in the range of 19.2 to 53.5 meV/atom and 16.9 to 54.9 meV/atom, respectively, indicating that universal MLIPs are less accurate compared to specialized MLIPs. Considering the lower computational efficiency of uMLIPs, it is concluded that the customized MLIPs employing traditional descriptors such as moment tensor, ACE (Drautz, 2019), and smooth overlap of atomic positions (SOAP) (Bartók et al., 2013) offer a more reliable and efficient approach than the uMLIPs.

For validation, the fundamental properties of four pure metals (Mo, Nb, Ta, and W)—including lattice constants, elastic constants, unstable stacking fault energy (USFE), and Peierls stress—were calculated using MTP14-new and MTP16-new. These results were then compared with those obtained from DFT and existing potentials such as MTP-Yin, MTP-Wang, and EAM-Zhou, as detailed in Table S1 and Fig. S1. Additionally, the generalized stacking fault energy (GSFE) curves of our new MLIPs were compared against those derived from EAM and DFT, as illustrated in Fig. S2. The findings demonstrate that the new MLIPs accurately predict the basic mechanical properties of these four pure metals.

Another noteworthy observation is the performance of the EAM potential, which consistently achieves a high MAE of 0.25 eV/atom across various datasets. Interestingly, in the AL-NPT-T/C dataset, the EAM achieves an MAE of 0.045 eV/atom, a figure comparable to that of other MLIPs as shown in Fig. 3(a). To further assess the accuracy of EAM, comparisons between EAM-Zhou and DFT calculations for energy of screw dislocations, AL-NPT-T/C, are illustrated in Fig. 3(b, c). Notably, EAM-Zhou accurately captures the trend of energy changes across all four pure elements in the screw dataset and demonstrates acceptable accuracy for $Mo_{25}Nb_{25}Ta_{25}W_{25}$ in the AL-NPT-T/C dataset. However, its performance significantly deteriorates for alloys with varying compositions for the screw dataset. Given that the composition of the MPEA is fixed for the AL-NPT-T/C dataset, our findings suggest that while EAM-Zhou may not reliably predict composition-induced energy changes, it performs effectively in simulations with a fixed composition. The observed inaccuracy in the simulation of alloys for the screw dataset likely arises from the inaccurate inter-element interactions within the EAM potential, which are determined through a universal mixing function. Later discussions in our paper will highlight that despite these limitations, EAM-Zhou's high computational efficiency renders it a viable option for large-scale simulations involving complex plasticity.

Furthermore, uncertainty quantification was conducted based on the D-optimality criterion and the MaxVol algorithm on a relaxed polycrystal for our MLIPs, as detailed in Fig. 3(d). The MLIP-3 package (Podryabinkin et al., 2023) is used to develop two MTPs (MTP3-existing, MTP3-all) for this purpose. The analysis reveals that MTP3-all significantly decreases the uncertainty in the polycrystal compared to MTP3-existing. Moreover, there are only 2 atoms with an extrapolation grade $\gamma > 2$ for MTP3-all, whereas there are 31 atoms with $\gamma > 2$ for MTP3-existing. These results highlight the substantial capability of our new MLIPs in modeling complex plastic deformation in MoNbTaW MPEAs.

4. Results

4.1. Basic mechanical property comparison: MPEAs versus constituent metals

Basic mechanical properties, such as elastic constants and GSFE, are crucial determinants of the mechanical strength of metals and alloys. To investigate the effect of composition, these properties were explored across the entire compositional space of MoNbTaW using MTP14-new. It is crucial to note that for MPEAs, statistical results are more informative than individual values of a property in understanding the behavior of these complex alloys. $Mo_{25}Nb_{25}Ta_{25}W_{25}$ is first used to illustrate the statistical distribution of basic properties, as depicted in Fig. 4. To better capture the variations in properties, all calculations are performed using a small supercell. To

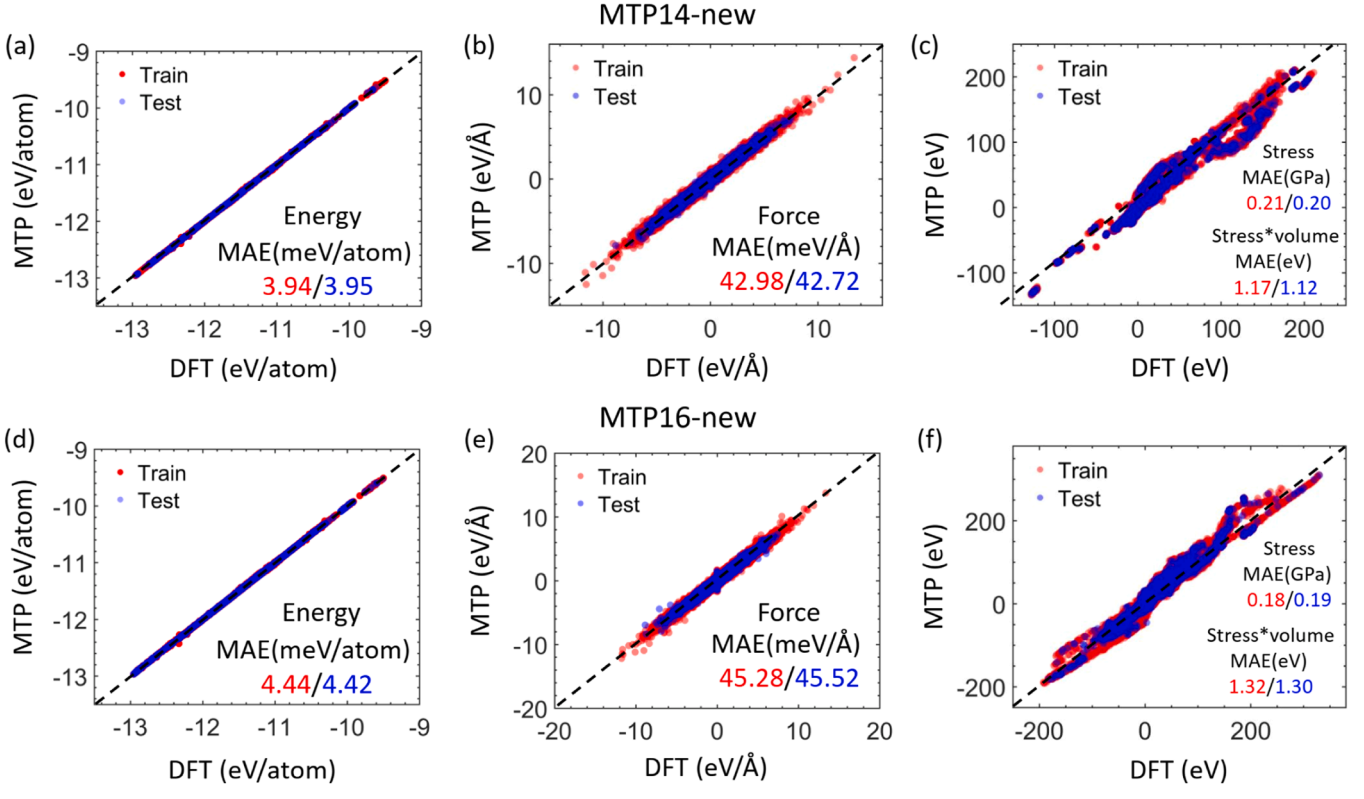

Fig. 2. MTP14-new (a-c) and MTP16-new (d-f) predictions on energies, forces, and stress for training and test datasets. In figures (c) and (f), the training and test errors are reported in both units of GPa (for stress) and eV (for stress*volume).

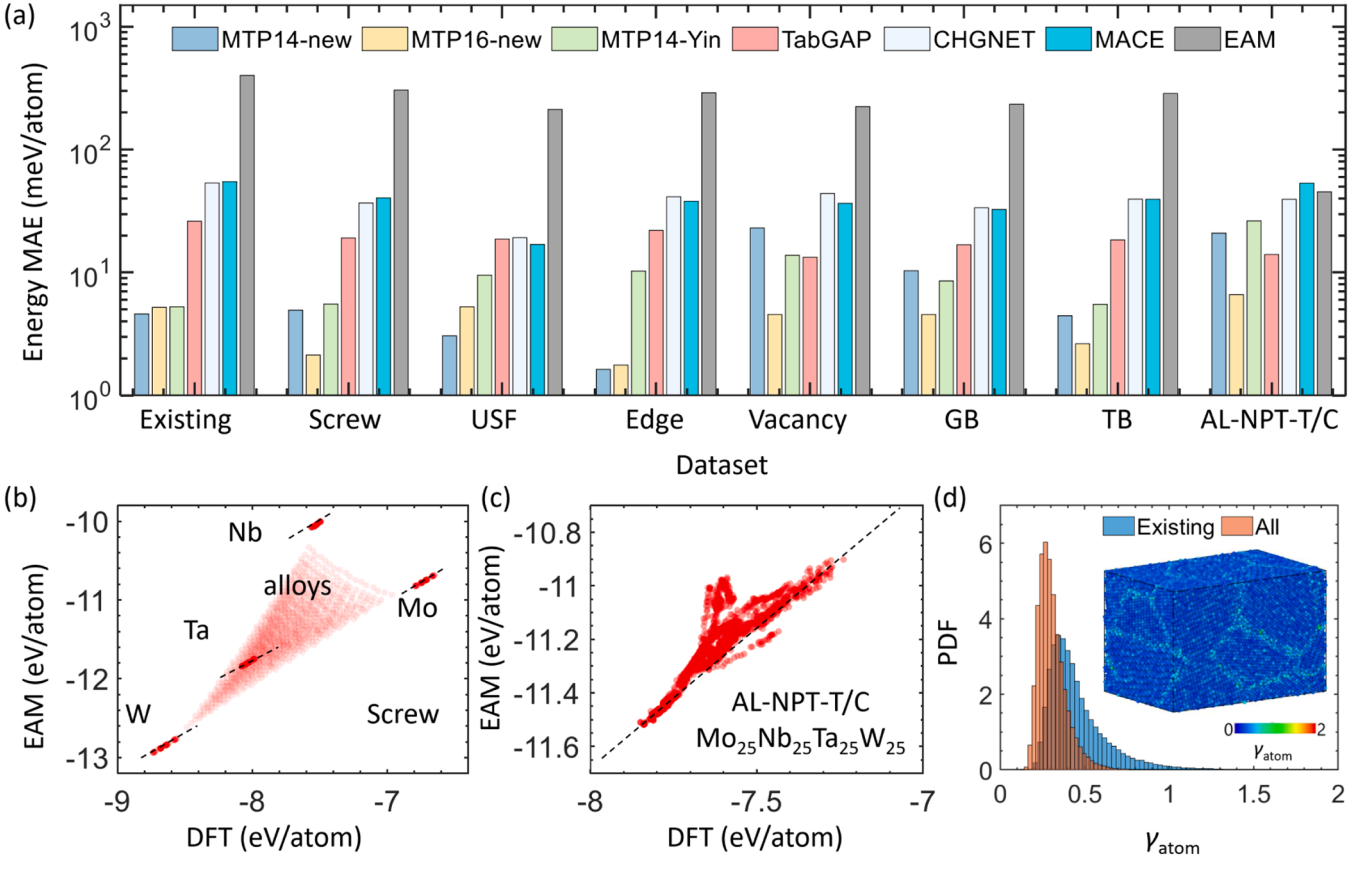

Fig. 3. (a) Comparison of energy prediction of different interatomic potentials using all DFT datasets. EAM prediction on energies for (b) screw and (c) AL-NPT-T/C datasets. (d) Uncertainty quantification using the D-optimality (MaxVol algorithm) in MLIP-3 (Podryabinkin et al., 2023). The inset displays a polycrystal with each atom color-coded according to the extrapolation grade (γ) based on the all dataset.

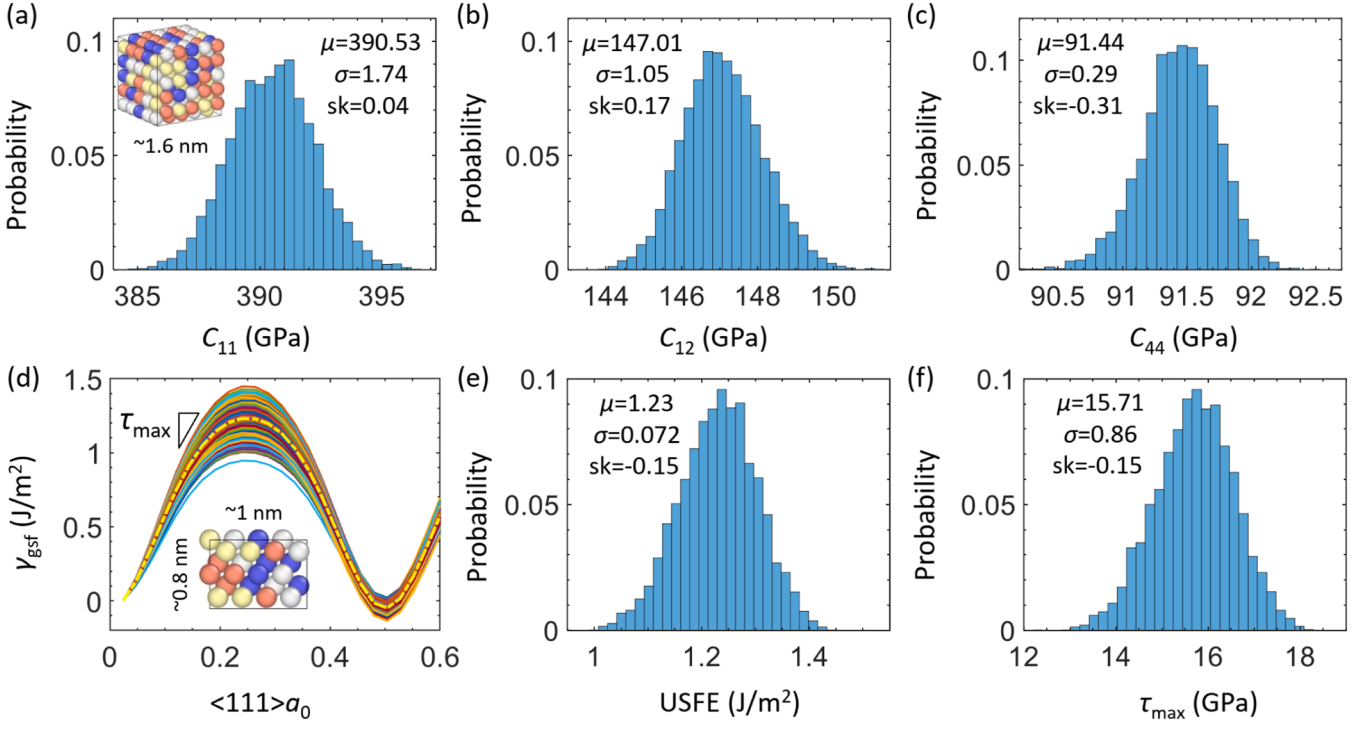

Fig. 4. (a-c) Statistical distribution of elastic constants C_{11}, C_{12} and C_{44} in $Mo_{25}Nb_{25}Ta_{25}W_{25}$. The inset in (a) displays the atomistic configuration used for elastic constant calculations. (d) Fluctuations of GSFE curves. The yellow dashed line represents the average GSFE curve. The inset in (d) shows the atomistic configuration used for GSFE calculations. (e, f) Statistical distribution of unstable stacking fault energy (USFE) and the maximum restoring force (τ_{max}).

explore the statistics of elastic constants and GSFE, 5000 random calculations are performed. For the GSFE calculations, energy minimization is carried out using the conjugate gradient (CG) algorithm, allowing only out-of-plane displacements during the relaxation process. Three independent elastic constants—C_{11}, C_{12}, and C_{44}—are presented in Fig. 4(a-c), where they exhibit a Gaussian-like distribution with relatively small standard deviations, indicating minimal variation due to the randomness of the chemical environment. Additionally, the fluctuations of GSFE curves were investigated using a small supercell with a cross-sectional area of around 0.8×1 nm^2; the results are shown in Fig. 4(d). The significant spread in GSFE curves is consistent with the previously recognized rough energy landscape for dislocation glide (Utt et al., 2022). The maximum restoring force is defined as the maximum gradient of GSFE curves, as shown in Fig. 4(d). Similarly, both USFE and the maximum restoring force (τ_{max}) follow a Gaussian distribution, as illustrated in Fig. 4(e, f). The ratios of the standard deviation to the average of the USFE and τ_{max} are 0.058 and 0.055, respectively, significantly higher than the corresponding ratio for the elastic constants, which is 0.0045. This indicates that local fluctuations in GSFE have a more pronounced effect on the mechanical properties of MPEAs compared to variations in elastic constants. It should be noted that these fluctuations are size-dependent. As the system size increases, the standard deviation approaches zero, in line with the previous simulation studies on FCC MPEAs (Zhao et al., 2019). It should be noted that such calculation area-dependent variation of GSFE is a statistical phenomenon that is independent of the underlying crystal structure.

The statistical distribution of the 287 compositions of MoNbTaW was then analyzed employing both MTP14-new and EAM potentials. These compositions span the entire compositional space, featuring a concentration interval of 10% for each element and including all equimolar combinations. The intriguing results reveal a robust correlation between τ_{max} and USFE (Fig. 5(a-c)), as well as between τ_{max} and elastic constants (Fig. 5(d-f)). Fig. S2 shows that the GSFE curves for pure elements are well-fitted by a sine function. This fitting strategy facilitates an analytical relationship between the peak values (USFE) and the maximum gradients of these curves (τ_{max}). Further analysis with MTP14-new identifies linear relationships between τ_{max} and USFE in terms of mean, standard deviation, and skewness, as depicted in Fig. 5(a-c). These findings indicate that τ_{max} and USFE are inherently related across various compositions. In contrast, slight deviations in these properties are observed with EAM, especially concerning standard deviation and skewness. Nevertheless, both MTP14-new and EAM-Zhou successfully capture the correlation between τ_{max} and USFE. Additional analyses are performed to explore the correlation between the average values of τ_{max} and the three elastic constants, as illustrated in Fig. 5(d-f). These results demonstrate a strong correlation between τ_{max} and C_{11} with MTP14-new, while EAM shows a significant correlation of τ_{max} with C_{44}, with the other correlations being relatively minor. By comparing values derived from EAM-Zhou and MTP14-new concerning GSFE and elastic constants, it is evident that EAM, despite some limitations, achieves reasonable accuracy.

Next, the influence of composition on the fundamental properties was investigated by evaluating the performance of the rule of mixing (ROM) in predicting their values. This enables a rational comparison of MPEAs with their constituent metals in terms of these fundamental properties. The average of a property P can be obtained by ROM as:

$$P_{ave} = \sum c_i P_i \tag{1}$$

where c_i denotes the concentration of element i, and P_i is the property of the same element. Similarly, the standard deviation of P can be calculated by ROM as:

$$P_{sd} = \sqrt{\sum_i c_i (P_i - P_{ave})^2} \tag{2}$$

Fig. 6(a) shows that ROM accurately predicts the average values of USFE obtained from MTP14-new. More intriguingly, the standard deviations of USFE and τ_{max} derived from ROM also exhibit a strong correlation with MTP14-new's predictions, as illustrated in Fig. 6(b, c). Additionally, Fig. 6(d-f) show that ROM effectively predicts the elastic constants C_{11} and C_{44}, though it shows significant deviations for C_{12}. These findings suggest that ROM is not only capable of predicting average values of USFE and elastic constants but also the standard deviations of USFE. This capability is particularly crucial for the rapid screening of mechanical properties in the expansive compositional space of MPEAs. By leveraging elemental concentration and properties, ROM allows for the prediction of properties of arbitrary compositions without the necessity for extensive new calculations.

More importantly, these results indicate that MPEAs do not inherently exhibit superior basic mechanical properties compared to their constituent metals, particularly with respect to the averages of USFE, $\tau_{max,}$ and elastic constants. Given that these fundamental properties generally adhere to ROM, the basic mechanical properties of MPEAs are bounded by those of the constituent metals. Nonetheless, the significantly higher strength observed in MPEAs, compared to their constituent metals, suggests that unique mechanisms, possibly stemming from compositional fluctuations, contribute to their enhanced macroscopic properties which is beyond what is obtained based on the traditional ROM approach.

4.2. Edge dislocation strengthening

One of the primary strengthening mechanisms in BCC MPEAs is edge dislocation strengthening (Lee et al., 2021; Maresca and Curtin, 2020a). Although MTP14-Yin bas been employed to investigate this in $Mo_{25}Nb_{25}Ta_{25}W_{25}$ (Yin et al., 2021), its accuracy regarding USFE and edge dislocation remains low, as indicated in Fig. 3(a). Consequently, it is imperative to utilize the MTP14-new to study edge dislocation strengthening in this system. The simple shear simulations were conducted using the PAD model containing an edge dislocation across 57 compositions (Table S2). The simulation setup, depicted in Fig. 7(a), includes lattice orientations, loading methods, and a wavy dislocation line. Each composition undergoes simulation five times with a random element distribution to determine the average critical shear stress, defined as the mechanical strength induced by edge dislocation. For illustration, the

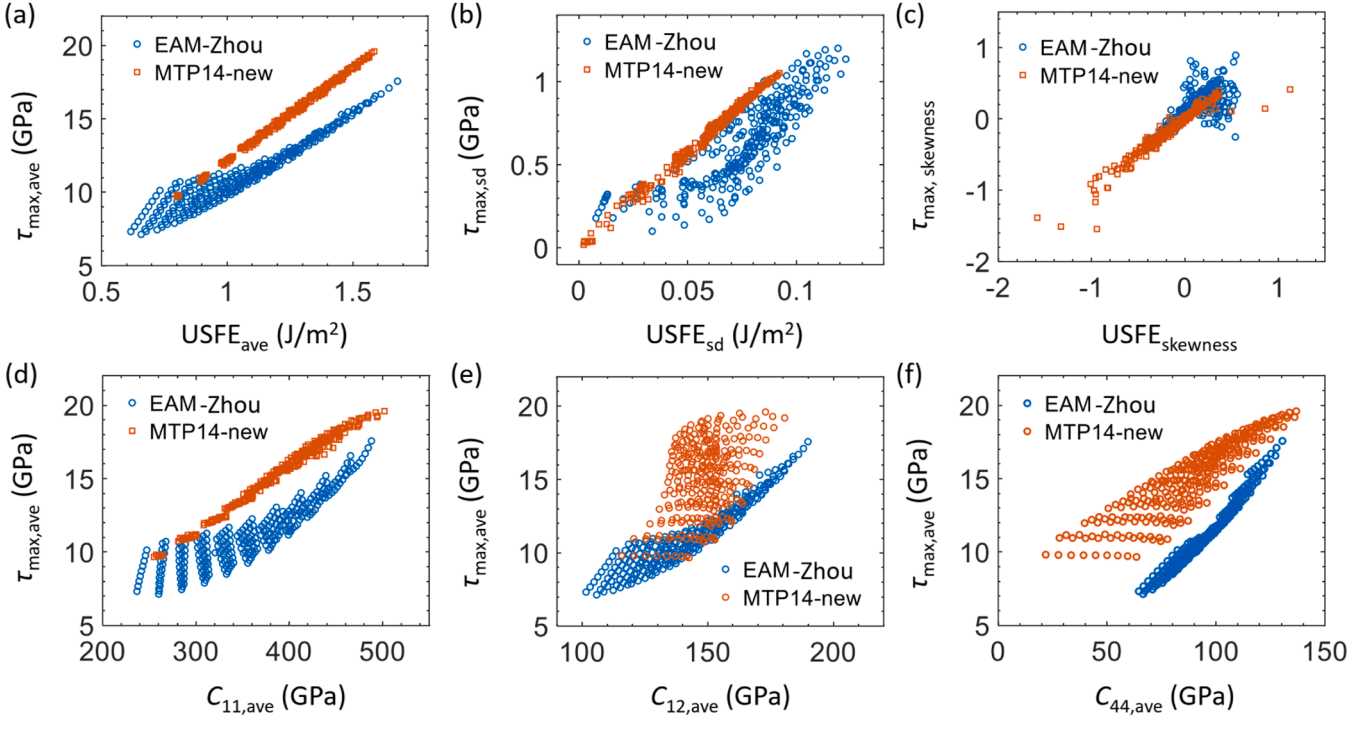

Fig. 5. Correlation (a-c) between the statistics of τ_{max} and USFE, as well as (d-f) between the statistics of τ_{max} and the elastic constant for 287 compositions.

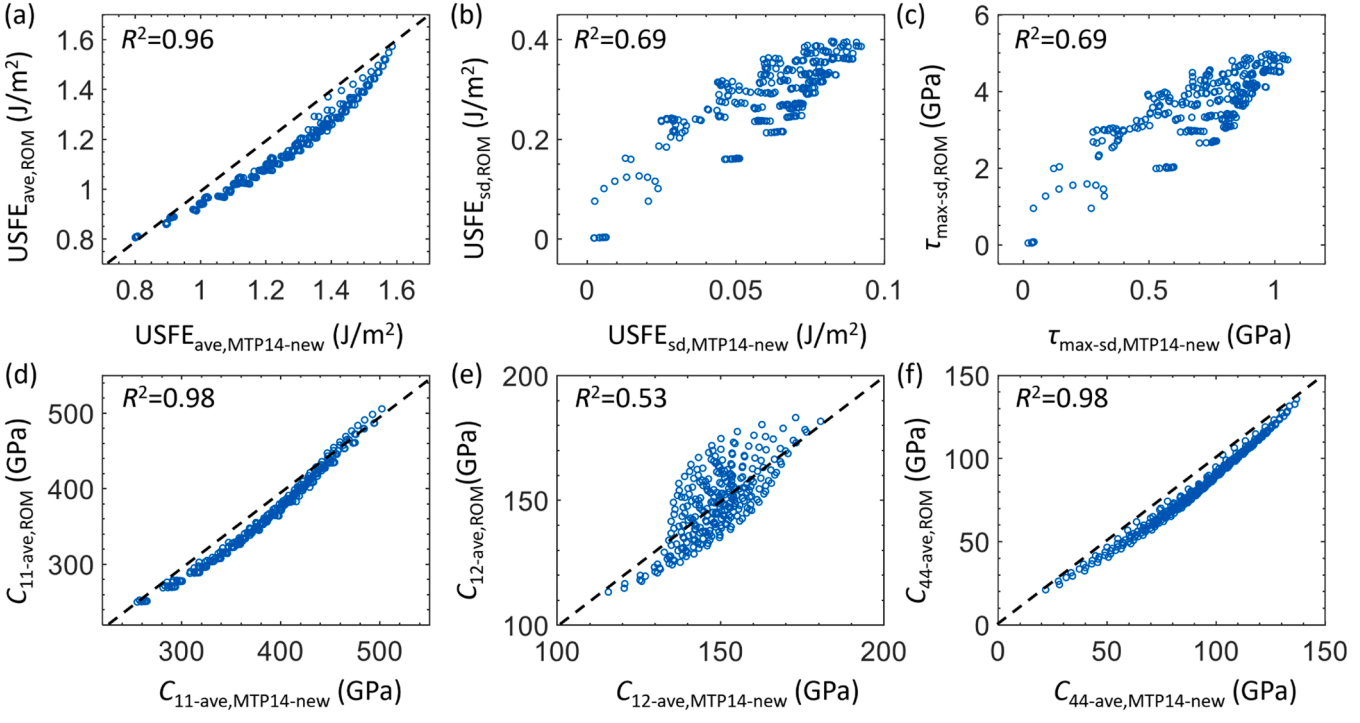

Fig. 6. Predictions of basic properties of 287 compositions compared to MTP14-new results using the rule of mixing (ROM). Dashed diagonal lines serve as a reference to visualize deviations between ROM-derived values and MTP14 predictions.

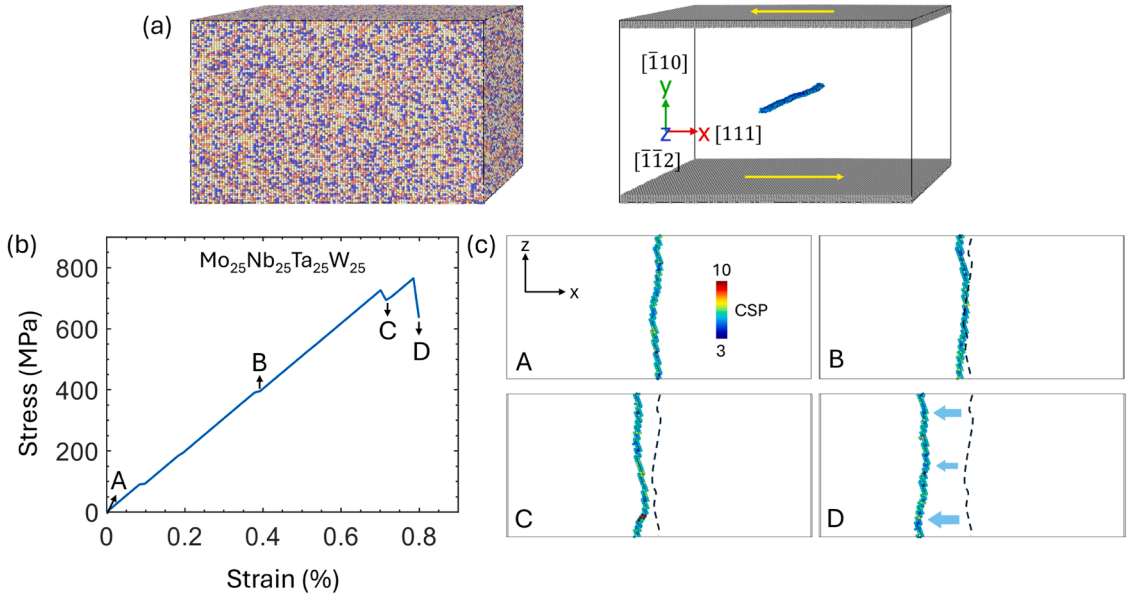

Fig. 7. (a) Simple shear model and wavy dislocation profile in $Mo_{25}Nb_{25}Ta_{25}W_{25}$. (b) Stress-strain curve with four critical points A-D labeled. (c) Edge dislocation profiles at four critical strains A-D. The centro-symmetry parameter (CSP) is used to represent the atomic environment of dislocation atoms.

stress-strain curve and corresponding dislocation profiles of $Mo_{25}Nb_{25}Ta_{25}W_{25}$ at different states are presented in Fig. 7(b, c). The panel A of Fig. 7(c) shows the wavy dislocation lines prior to any loading. With continues loading, it is observed that the partial glide of dislocations results in a slight deviation in the curve at point B. Further loading up to point C causes the entire dislocation line to move in the negative *x*-direction, with additional loading at point D resulting in an increased glide distance for the entire dislocation. The critical shear stress, determined to be 780 MPa in this instance, is significantly higher than that of the constituent elemental metals listed in Table S1, thereby highlighting the exceptional edge dislocation strengthening observed.

We then compare the edge dislocation strengthening (S_{edge}) in 57 compositions using the EAM and MTP14-new, with the results presented in Fig. 8. Despite variations in absolute values, a strong correlations is observed between their prediction values. Given that MTP14-new is meticulously trained using DFT datasets of USF and edge dislocation across the compositional space, the predicted mechanical strength should approach the accuracy of DFT. Our comparison between MTP14-new and EAM indicates that EAM, despite its lower accuracy in predicting inter-element interactions (Fig. 3), effectively captures the fundamental physics of edge dislocation strengthening across different compositions. This is particularly significant as most existing computational studies on MPEAs utilize the EAM potential. Our results in Fig. 8 thus validate the reliability of these studies using EAM potentials, at least for MoNbTaW systems.

By analyzing the mechanical strength of each composition and correlating it with the basic properties, valuable insights can be gained into the exceptional strength of MPEAs compared to their constituent metals. For both EAM and MTP14-new, the strong correlations between the strength (S_{edge}) and the standard deviation of USFE ($USFE_{sd}$) are observed, as evidenced by the values from interatomic potentials (Fig. 9(a, d)) and values predicted by the principle of ROM (Fig. 9(b, e)). However, the correlation between the

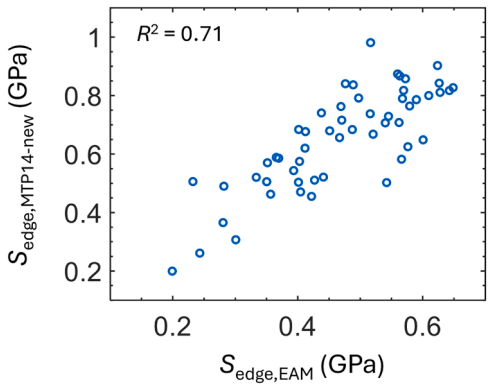

Fig. 8. Comparison of edge dislocation strengthening between MTP14-new and EAM potentials.

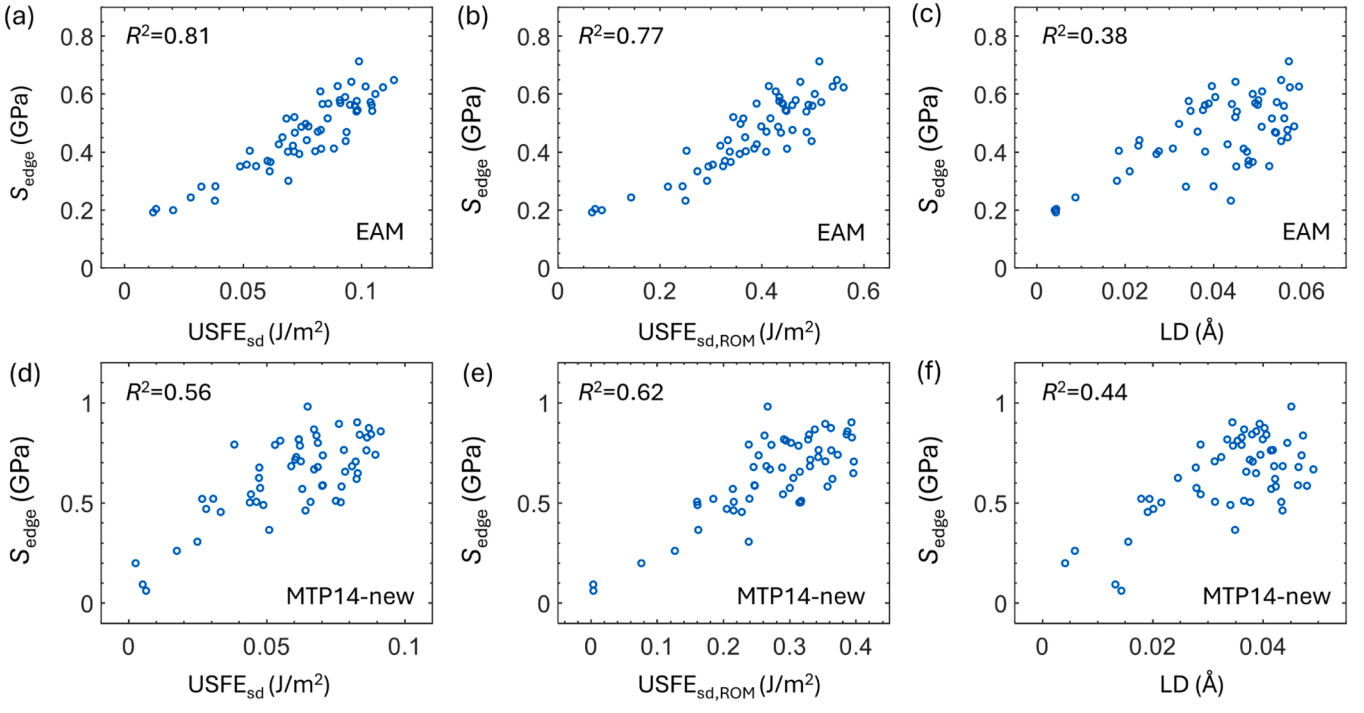

Fig. 9. Correlation between the edge dislocation strengthening and the basic properties in MPEAs using EAM and MTP14-new. (a-c) EAM; (d-f) MTP14-new.

strength and the lattice distortion (LD) is relatively low for both the potentials, as shown in Fig. 9(c) for EAM and Fig. 9(f) for MTP14-new. These findings suggest that LD, traditionally used as an indicator (Okamoto et al., 2016; Su Sohn et al., 2019), is less effective than the newly identified $USFE_{sd}$ in predicting the MPEA strength.

Additionally, the current strength data of 57 compositions was employed to validate the well-developed solid solution strengthening (SSS) model from Maresca & Curtin (Lee et al., 2021; Maresca and Curtin, 2020a):

$$S_{SSS} = 0.04\alpha^{-\frac{1}{3}}\mu\left(\frac{1+\nu}{1-\nu}\right)^{\frac{4}{3}}\left[\frac{\Sigma_n c_n \Delta V_n{}^2}{b^6}\right]^{\frac{2}{3}} \tag{3}$$

where α is the dislocation line tension parameter, which is a constant for a given type of dislocation, μ is the shear modulus, ν is the Poisson' ratio, c_n is the concentration of element n, and b is the magnitude of Burgers vector. ΔV_n is the misfit volume obtained from the rule of mixing. Another LD-based empirical model has been proposed as (Tandoc et al., 2023):

$$S_{LD} \sim \mu * \mathrm{USFE} * \mathrm{LD} \tag{4}$$

It should be noted that Eq. (4) is derived from Eq. (3), a simplified linear model that establishes a direct relationship between the mechanical strength of MPEAs and LD. For a more accurate evaluation, this model incorporates both the elastic properties (μ) and the resistance to dislocation glide, i.e, USFE. Recent studies have identified S_{LD} as an effective indicator of yield strength and hardness in BCC refractory MPEAs (Tandoc et al., 2023). Fig. 10(a, b) indicate that S_{LD} shows weak correlation with S_{edge} for EAM, whereas there is a strong correlation between S_{LD} and S_{edge} for MTP14-new across all the 57 compositions. The weak correlation between S_{LD} and S_{edge} for EAM likely stems from inaccurate calculations of LD. Furthermore, Fig. 10(c, d) demonstrate that Eq. (3) works well for both EAM and MTP14-new. The effectiveness of Eq. (3) in EAM is attributed to the fact that the critical quantity in this model, the misfit volume, is derived from the elemental atomic volumes using ROM. Moreover, Eq. (4) shows better predictability than Eq. (3) for MTP14-new, suggesting that it is more effective in predicting edge dislocation strengthening, possibly because LD in Eq. (4) incorporates more informative insights than the misfit volume in Eq. (3).

Despite the effectiveness of the solid solution strengthening model (Eq. (3)) and the LD-based (Eq. (4)) model in predicting the strength of MPEAs, the newly identified indicators—namely the standard deviation of USFE ($USFE_{sd}$) and the maximum restoring force ($\tau_{max,sd}$)—present an alternative approach. One advantage of $USFE_{sd}$ and $\tau_{max,sd}$ is that their values can be readily estimated using ROM, enabling the fast screening of mechanical strength of MPEAs in the vast compositional space. Additionally, their physical rationale is grounded in the PN model, which correlates the Peierls stress with τ_{max} or USFE. In MPEA systems characterized by

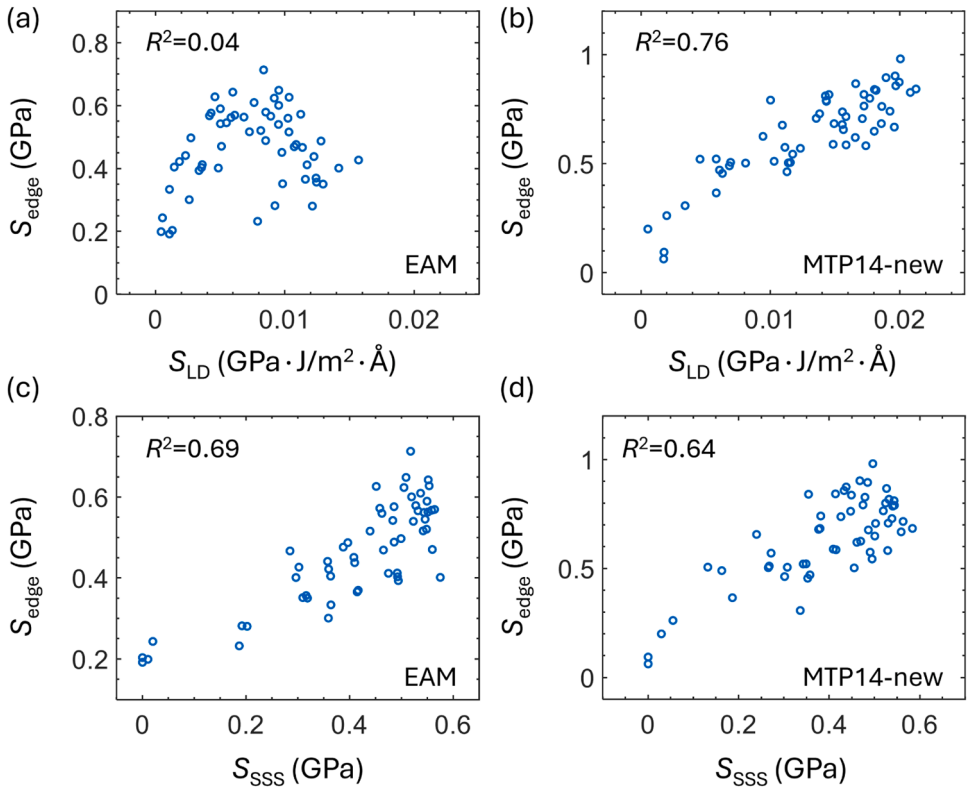

Fig. 10. Validation of (a, b) lattice distortion (LD)-based model and (c, d) solid solution strengthening (SSS) model in predicting the edge dislocation-induced strength in MPEAs.

fluctuating energy landscape, as explored in another recent study of ours (Shuang et al., 2025), $USFE_{sd}$ plays a pivotal role in impeding dislocation glide by creating a highly irregular Peierls energy landscape.

4.3. Grain boundary-mediated strengthening

Next, the GB-mediated deformation mechanism was examined. The newly developed MTP16-new allows us to explore complex deformation mechanisms, such as polycrystal compression. Using both MTP16-new and EAM, the plastic deformation of such cases was investigated as depicted in Fig. 11(a). The polycrystal model contains 6 grains and 91,544 atoms with the average grain size of 6.5 nm. A strain rate of 5×10^8 s^{-1} (5e8 s^{-1}) is applied for both MTP16-new and EAM at a temperature of 300 K, while a lower strain rate of 1.5×10^7 s^{-1} (1.5e7 s^{-1}) is used exclusively in the case of EAM to mitigate the effects of extremely high strain rates in MD simulations. Fig. 11(b) presents the stress-strain curves for the four constituent elements and $Mo_{25}Nb_{25}Ta_{25}W_{25}$ using MTP16-new. It is observed that W exhibits the steepest slope during the elastic stage and the highest flow stress during the plastic stage. Ta and Nb display the lowest slope and flow stress. Interestingly, $Mo_{25}Nb_{25}Ta_{25}W_{25}$ and Mo show similar slope and flow stresses, positioned between those of W and Ta. The plastic deformation histories at points A, B, and C are illustrated in Fig. 11(a), revealing that the deformation is primarily governed by GB sliding up to point B, with only minimal dislocation activities observed until point C. This indicates that GB-mediated deformation is the dominant mechanism throughout the entire process, attributed to the small grain size used in the current simulations.

MD simulations were then extended to include additional 38 compositions of MPEAs (Table S3) using both MTP16-new and EAM using the strain rate of 5×10^8 s^{-1} (5e8 s^{-1}) at 300 K. Interestingly, as shown in Fig. 11(c), the strength for all these compositions exhibits a strong correlation between the EAM and MTP16-new results. Additionally, ROM was employed to estimate the strength of each composition based on the strength of constituent metals and their elemental concentrations. The results, depicted in Fig. 11(d, e), indicate that ROM predictions closely match the actual values at both high (5×10^8 s^{-1}) and low (1.5×10^7 s^{-1}) strain rates for EAM. A similar conclusion is reached with the MTP16-new model, as illustrated in Fig. 11(f). Given the high accuracy of the MTP16-new, it is safe to conclude that MPEAs do not exhibit superior strength compared to their constituent elements in the compression of nano-polycrystals, and both the simple EAM and the more precise MTP16-new potentials are capable of capturing these critical mechanisms. The strength superiority of MPEAs and their constituent metals are opposite from the edge dislocation strengthening in Section 4.2.

Combining the extensive simulations presented in Sections 4.1–4.3, it is evident that although EAM-Zhou does not replicate the energy values as accurately as DFT (see Fig. 3), the mechanical properties of pure metals and MPEAs obtained from EAM closely align with those derived from our newly developed MTPs. This includes a range of properties such as elastic constants, USFE, edge dislocation strengthening, and compression of nano-polycrystals. These results demonstrate the fidelity of EAM-Zhou in modeling complex plastic deformation in MoNbTaW MPEAs. Given the exceptional computational efficiency of EAM, it will exclusively be used for extremely large-scale simulations in the following section, which involve tens of millions of atoms.

4.4. Large-scale simulations using EAM potential

Initially, results from the compression of a nanopillar are presented. The nanopillar features a ⟨100⟩ axis orientation, a diameter of 50 nm, a height of 100 nm, and comprises 12,012,001 atoms. The axis direction is periodic, while the other two directions are free. The simulations are conducted at a temperature of 300 K, and a strain rate of 10^8 s^{-1} is applied for pure W and $Mo_{25}Nb_{25}Ta_{25}W_{25}$. An NVT (canonical) ensemble is utilized during the compression simulations. To investigate the effect of lattice distortion, the same simulation was conducted using the average-atom (A-atom) potential (Varvenne et al., 2016b). As illustrated in Fig. 12(a), the W nanopillar exhibits a steeper slope during the elastic stage, indicating a higher elastic modulus, along with higher yielding and flow stresses compared to the $Mo_{25}Nb_{25}Ta_{25}W_{25}$ nanopillar. Interestingly, the strength observed in these materials contrasts with the experimental findings which typically show greater strength in $Mo_{25}Nb_{25}Ta_{25}W_{25}$ than in pure W during nanopillar compression (Zou et al., 2014). Moreover, the A-atom nanopillar exhibits higher yielding strength than $Mo_{25}Nb_{25}Ta_{25}W_{25}$. However, both the cases display very similar flow stress at the early stage of plastic deformation. When the strain exceeds 0.15, $Mo_{25}Nb_{25}Ta_{25}W_{25}$ shows slightly higher flow stress than the A-atom. These results suggest that while lattice distortion in $Mo_{25}Nb_{25}Ta_{25}W_{25}$ reduces its yielding stress and does not significantly affect the early stages of plastic deformation, it provides a minor strengthening effect when the strain exceeds 0.15.

Fig. 12(b) presents the microstructures formed at the end of the compression. In the $Mo_{25}Nb_{25}Ta_{25}W_{25}$ nanopillar, numerous dislocations are visible between slip bands formed through deformation twinning and TB migration. There are several major mature slip bands, leading to the shearing of the nanopillar. Similarly, the A-atom nanopillar form several mature slip bands. The fewer dislocation lines in the A-atom nanopillar can be attributed to the absence of lattice distortion. In contrast, the W nanopillar exhibits numerous immature slip bands and short dislocation lines. These short lines, which are unidentified in OVITO, indicate severe plastic deformation within TBs. The differences in plastic mechanisms between $Mo_{25}Nb_{25}Ta_{25}W_{25}$ and pure W explain the discrepancy in the strength of these two materials.

Although polycrystal compression simulations are discussed in Section 4.3, the limited dimensions of these simulations resulted in deformation being predominantly influenced by GB sliding and migration. To better assess the role of dislocations in the deformation of polycrystals, the EAM was employed to conduct simulations using a significantly larger-scale polycrystal model (containing 5,859,403 atoms), as presented in Fig. 13(a). The model contains 12 grains, and the average grain size is 20.0 nm. The strain rate is 1×10^8 s^{-1} and the simulation temperature is 300 K. The stress-strain curves, shown in Fig. 13(b), indicate that pure W consistently exhibits higher yielding stress and flow stress than both $Mo_{25}Nb_{25}Ta_{25}W_{25}$ and the A-atom cases throughout the entire deformation

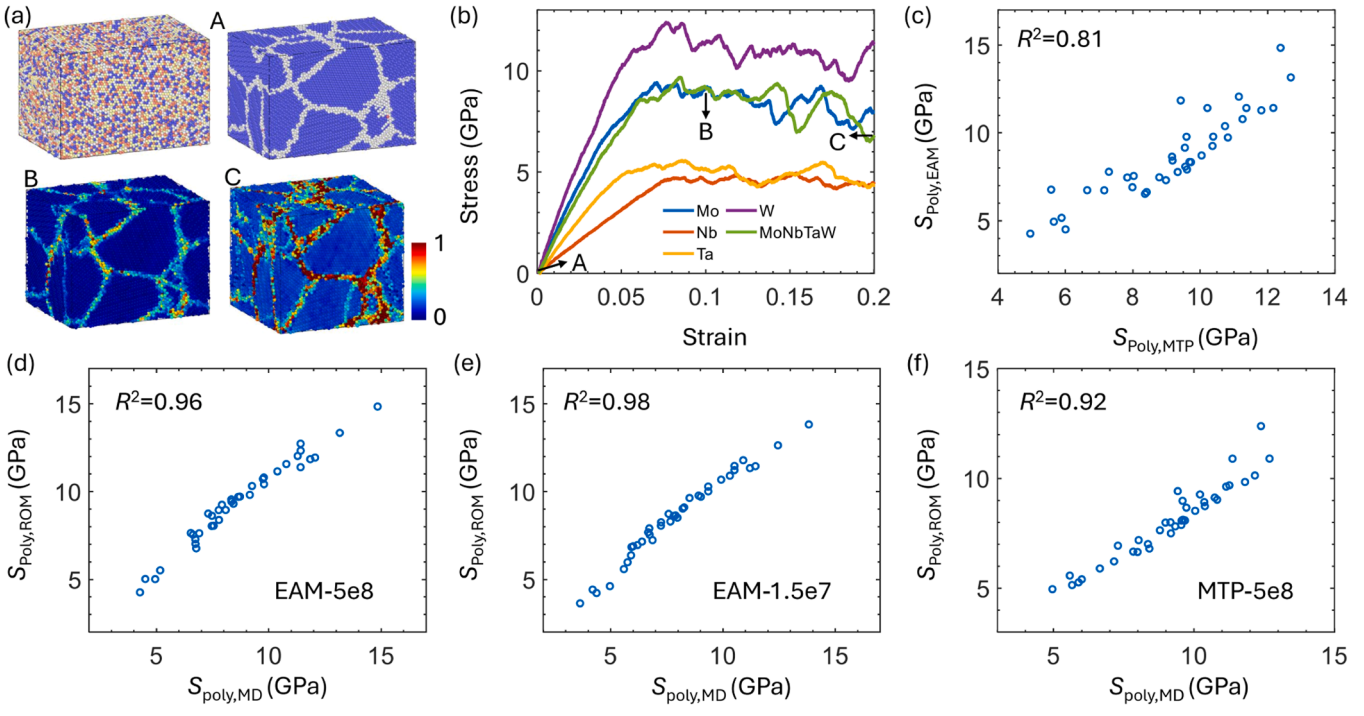

Fig. 11. (a) Atomic shear strain at different strains of polycrystal $Mo_{25}Nb_{25}Ta_{25}W_{25}$ (abbreviated as MoNbTaW). (b) Stress-strain curves of the four pure metals and $Mo_{25}Nb_{25}Ta_{25}W_{25}$ obtained using MTP16-new. (c) Comparison of strength between EAM and MTP16-new results. (d-f) Comparison of strength between predictions from rule of mixing (ROM) and the values from EAM and MTP16-new.

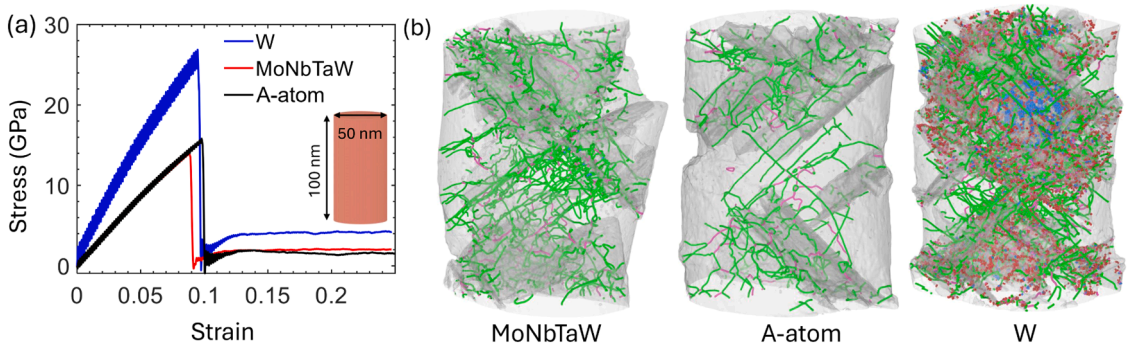

Fig. 12. Large-scale compression simulations of single-crystalline nanopillar of W and $Mo_{25}Nb_{25}Ta_{25}W_{25}$ (abbreviated as MoNbTaW). (a) Stress strain curves. (b) Dislocations and defects at the end of deformation. The green, pink, and red lines represent 1/2<111> dislocations, ⟨100⟩ dislocations, and other dislocations. The interior gray interfaces represent TBs.

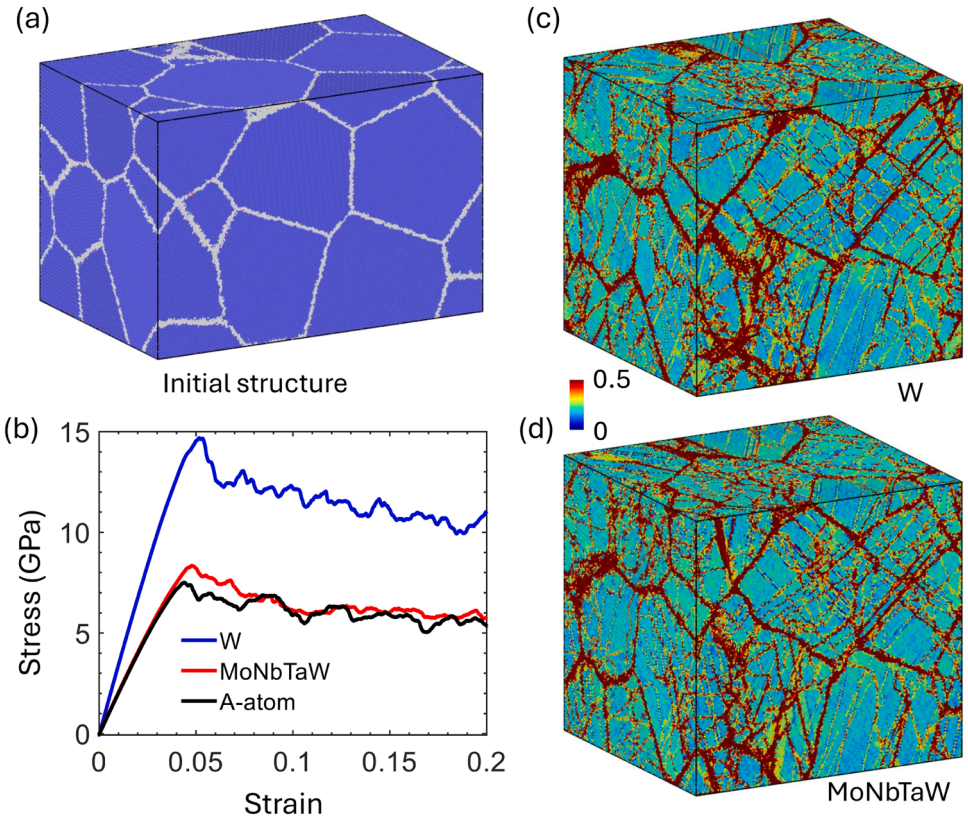

Fig. 13. Large-scale compression simulations of polycrystal W, $Mo_{25}Nb_{25}Ta_{25}W_{25}$ (abbreviated as MoNbTaW) and A-atom. (a) Polycrystal with GBs are identified by common neighbor analysis. (b) Stress-strain curves. (c, d) Atomic shear strain for W and $Mo_{25}Nb_{25}Ta_{25}W_{25}$ at the end of deformation. All atoms are colored by the atomic shear strain, which represents the plastic slip history.

process. Fig. 13(c, d) illustrate the slip history of the polycrystal models, demonstrating that dislocation activities are highly active during compression for both the systems. Notably, the A-atom model exhibits slightly lower stress levels than $Mo_{25}Nb_{25}Ta_{25}W_{25}$ due to the absence of lattice friction.

Another commonly used approach is the instrumental indentation technique, which has been widely used to obtain the mechanical properties of MPEAs (Wang et al., 2024b). We employ a spherical indenter in our nanoindentation simulation, with results presented in Fig. 14. It is observed that both the load and hardness of pure W are significantly higher than those of $Mo_{25}Nb_{25}Ta_{25}W_{25}$ throughout the entire loading and holding stages, indicating that W is harder than $Mo_{25}Nb_{25}Ta_{25}W_{25}$ (see Fig. 14(a, b). This finding is unexpected, as previous experiments have indicated the opposite trend (Zou et al., 2014). Fig. 14(c, e) display the dislocation profiles beneath the indenter at the end of the holding stage, while Fig. 14(d, f) depict the plastic slip history during the loading and holding stages for

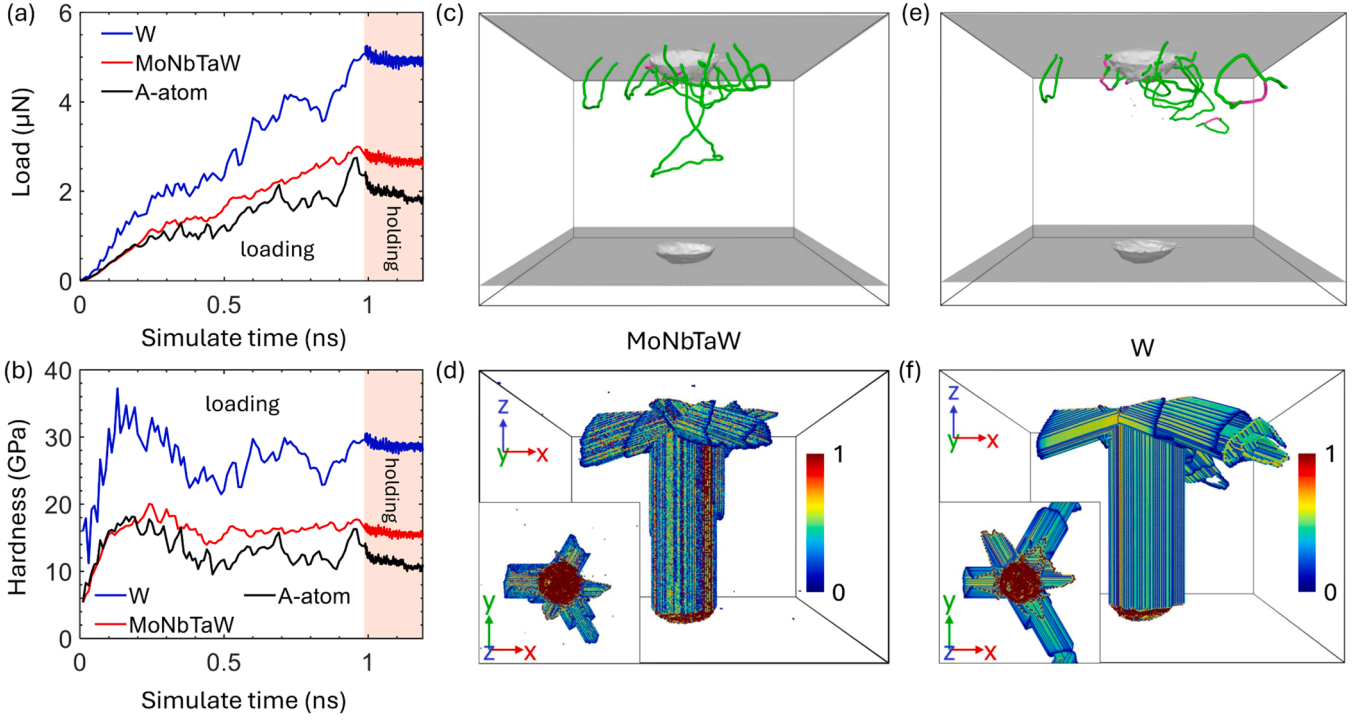

Fig. 14. Nanoindentation simulations of W and $Mo_{25}Nb_{25}Ta_{25}W_{25}$ (abbreviated as MoNbTaW) using a spherical indenter. (a, b) Evolution of load and hardness. (c, d) Dislocation network and plastic slip history at the end of holding stage in $Mo_{25}Nb_{25}Ta_{25}W_{25}$. (e, f) Dislocation network and plastic slip history at the end of holding stage in W.

$Mo_{25}Nb_{25}Ta_{25}W_{25}$ and pure W, respectively. These atomistic observations reveal no significant differences in the deformation mechanisms between the two materials. A-atom shows the noticeable decrease of load and hardness compared to $Mo_{25}Nb_{25}Ta_{25}W_{25}$, indicating that lattice distortion strengthening has more effect in this case than previous simulations in Figs. 12 and 13. It should be noted that the unusually high hardness value observed for W (approximately 40 GPa) can be attributed to factors such as the absence of initial defects, the high strain rate, and the small indenter radius used in MD simulations. A similar hardness value was reported for BCC W in (Domínguez-Gutiérrez et al., 2023).

5. Discussion

In this study, new MLIPs have been developed which are applicable for general plastic deformation mechanisms in MoNbTaW MPEAs and benchmarked them against the existing EAM potential. This enables us to effectively examine the mechanical strength of MoNbTaW systems across various compositions. The central theme of this paper is the critical assessment of the presumed superiority of MPEAs over constituent metals in terms of mechanical strength. MPEAs are commonly believed to exhibit high strength due to severe lattice distortion. We evaluate this viewpoint using DFT-accurate machine-learning atomistic simulations and reliable large-scale EAM-based simulations. All strengths of MoNbTaW and W in previous experiments and our simulations are summarized in Table 1. Our simulation results suggest that the mechanical strength of MoNbTaW does not always surpass that of constituent metals; rather, its effectiveness depends on the specific plastic mechanisms and the involved length scale. Specifically, MPEAs excel over constituent metals primarily when solid solution strengthening is dominant, with dislocation motion being prevalent. The superior intrinsic strength of MPEAs, relative to their constituent metals, is evidenced by our shear stress-driven dislocation motion simulations in Section 4.2. This finding is further supported by consistent observations in prior simulations (Li et al., 2019a; Yin et al., 2021), theoretical predictions (Maresca and Curtin, 2020a), and experimental studies (Zou et al., 2015, 2014). However, for other mechanisms such as dislocation nucleation, and GB-mediated deformation, constituent metals like W consistently outperform MoNbTaW. Our MD simulation results, which include single crystal compression, nanoindentation, and polycrystal compression, as presented in Sections 3 and 4, together with the majority of prior MD simulations on MPEAs and pure metals, consistently support this conclusion. This length scale and plasticity mechanism-dependent superiority can be rationalized by the well-recognized size-dependent deformation mechanisms in metals. In this section, the established mechanistic models will be employed to analyze these effects.

Theoretically, the overall strength in a bulk crystalline metal can be attributed to the syngenetic effects of various mechanisms (Li et al., 2021):

$$\sigma_y = \sigma_{\text{fr}} + \sigma_{\text{ss}} + \sigma_{\text{forest}} + \sigma_{\text{GB}} + \sigma_{\text{pp}} + \sigma_{\text{tb}} + \sigma_{\text{ph}} \tag{5}$$

where σ_{fr} is the lattice friction, σ_{ss} is the solid solution strength. It should be noted that lattice friction and solid solution strength are somewhat ambiguous concepts in MPEAs, as distinguishing solute atoms from the matrix is particularly challenging. Therefore, the approach of the stochastic Peierls Nabarro model (Shuang et al., 2025; Zhang et al., 2019) is adopted and these factors are collectively considered as the intrinsic strength of MPEAs ($\sigma_{\text{intrinsic}} = M\tau_{\text{intrinsic}}$, where $M = 2.7$ is the Taylor factor converting the shear stress to the normal stress). The term σ_{forest} accounts for the dislocation forest hardening which has the form of $\sigma_{\text{forest}} = \alpha MGb\sqrt{\rho}$, where α is a constant falling in the range 0.1 to 1.0, G is the shear modulus, b is the magnitude of burger vector, and ρ is the dislocation density. σ_{GB} represents GB strengthening, known as the Hall-Patch effect, which can be expressed as $\sigma_{GB} = Mkd^{-0.5}$, where k is the Hall-Petch slope. σ_{pp}, σ_{tb} and σ_{ph} represent precipitation strengthening, twin boundary strengthening, and phase-transformation-induced strengthening, respectively. For simplicity, only the first four mechanisms in Eq. (5) were considered since they are normally presented in all polycrystalline alloys, allowing us to express the strength of MPEAs or constituent metals as follows:

$$\sigma_y = M\tau_{\text{intrinsic}} + \alpha MGb\sqrt{\rho} + Mkd^{-0.5} \tag{6}$$

On the other hand, for a single-crystalline micro/nano pillar, the strength can be written as (Zou et al., 2015):

$$\sigma_y = M\tau_{\text{intrinsic}} + \alpha MGb\sqrt{\rho} + \sigma_{\text{source}} \tag{7}$$

where $\sigma_{\text{source}} = MKG\frac{\ln(\bar{\lambda}/b)}{\bar{\lambda}/b}$ represent the dislocation nucleation-dominated strength, K is the source-strengthening constant in the order of 0.1 (Rao et al., 2007), $\bar{\lambda}$ is the average source length which can be estimated by the pillar diameter D (Zou et al., 2014). The choice to

Table 1
Summary of strengths of MoNbTaW and W in previous experiments and our simulations. Note that the strength values for single-crystalline (SC) nanopillar compression from previous experiments (Zou et al., 2014) correspond to the stress at a strain of 8% for pillars with a diameter of 200 nm.

	Loading conditions	MoNbTaW (MPa)	W (MPa)
Exp	Hardness (Zou et al., 2014)	4850	3710
	SC nanopillar compression (Zou et al., 2014)	1400	1100
Sim	Single edge dislocation motion	780	20
	SC nanopillar compression	2000	4000
	Polycrystal compression using MTP16-new	9000	11,000
	Polycrystal compression using EAM	7000	12,000
	SC nanoindenation using EAM	16,000	28,000

use the source-strengthening constant of 0.1 is informed by its alignment with the strength predictions of $Mo_{25}Nb_{25}Ta_{25}W_{25}$ found in previous experimental data (Zou et al., 2014). Moreover, another study further supports that nucleation barriers in MPEAs are lower than in pure metals (Xiao et al., 2020). Therefore, applying the constant 0.1 likely results in an overestimation of dislocation nucleation in MPEAs. Despite this, such an overestimation does not alter our primary conclusions. Due to the inherently smaller K value for MPEAs, any potential overestimation leads to an earlier transition in the diminishing strength of MPEAs as the size decreases. This underpins our argument and the overall findings presented in this study.

Our analysis primarily focuses on comparing $Mo_{25}Nb_{25}Ta_{25}W_{25}$ and W, with special emphasis on W due to its higher strength than other elements (Mo, Nb and Ta) and extensive experimental validation. Our results, presented in Section 4.1, affirm that the basic mechanical properties of MoNbTaW MPEAs consistently adhere to ROM across their entire compositional range. Specifically, W shows the highest shear modulus at 164 GPa (Suzuki et al., 1999), while Nb exhibits the lowest at 47.2 GPa (Duesbery and Vitek, 1998). The shear modulus of $Mo_{25}Nb_{25}Ta_{25}W_{25}$ alloy is approximately 114 GPa (Zou et al., 2014). The significant discrepancy in shear modulus between W and $Mo_{25}Nb_{25}Ta_{25}W_{25}$ suggests a potential role of forest hardening (σ_{forest}) and source hardening (σ_{source}) in Eqs. (6) and (7) in enhancing the strength of W, thereby making it superior than that of $Mo_{25}Nb_{25}Ta_{25}W_{25}$. For the forest hardening, the strength difference σ_{forest}(W)-σ_{forest} ($Mo_{25}Nb_{25}Ta_{25}W_{25}$) was plotted as a function of dislocation density in Fig. 15(a). It is observed that due to the higher shear modulus in W, it consistently exhibits higher forest hardening-induced strength than $Mo_{25}Nb_{25}Ta_{25}W_{25}$. Within the dislocation density range observed in experiments ($1\times10^{12} \sim 3\times10^{14}$ m^{-2}), W exhibits an additional forest hardening-induced strength ranging from 0.02 GPa to 0.25 GPa compared to $Mo_{25}Nb_{25}Ta_{25}W_{25}$ (indicated by the green box in Fig. 15(a)).

It is also noted that BCC metals typically exhibit a higher Peierls stress for screw dislocations than for edge dislocations, which leads to the high intrinsic strength but low ductility at low temperatures. Consequently, the intrinsic strength difference between W and $Mo_{25}Nb_{25}Ta_{25}W_{25}$ is insignificant at low temperature. For W, $\sigma_{intrinsic} = 793.8$ MPa at 300 K (Lee and Nix, 2012), with a Hall-Petch slope (k) of 1000 MPa$\sqrt{\mu m}$ (Cordero et al., 2016). For $Mo_{25}Nb_{25}Ta_{25}W_{25}$, k is available from experiments directly. However, recent experiments obtained k values ranging from 1462 to 1774 MPa$\sqrt{\mu m}$ for $Mo_{20}Nb_{20}Ta_{20}V_{20}W_{20}$ (Kang et al., 2018), and another study assumed $k = 1700$ MPa$\sqrt{\mu m}$ for $Mo_{25}Nb_{25}Ta_{25}W_{25}$, achieving good agreement in strength prediction between theory and experiments (Zou et al., 2015). Based on these experiments and the observation that MPEAs typically exhibit higher k values than pure metals, a k value of 1700 MPa$\sqrt{\mu m}$ was adopted for $Mo_{25}Nb_{25}Ta_{25}W_{25}$ in this study. Based on the previous experiments (Senkov et al., 2011), $\sigma_{intrinsic} = 950$ MPa was obtained for $Mo_{25}Nb_{25}Ta_{25}W_{25}$ at 300 K, which is slightly higher then W at 300 K. It should be noted that $Mo_{25}Nb_{25}Ta_{25}W_{25}$ exhibits superior strength than W at higher temperatures. For example, $\sigma_{intrinsic} = 178.2$ MPa for W at 600 K, while $\sigma_{intrinsic} = 780$ MPa for $Mo_{25}Nb_{25}Ta_{25}W_{25}$ at the same temperature (Maresca and Curtin, 2020a), attributed to the unique edge

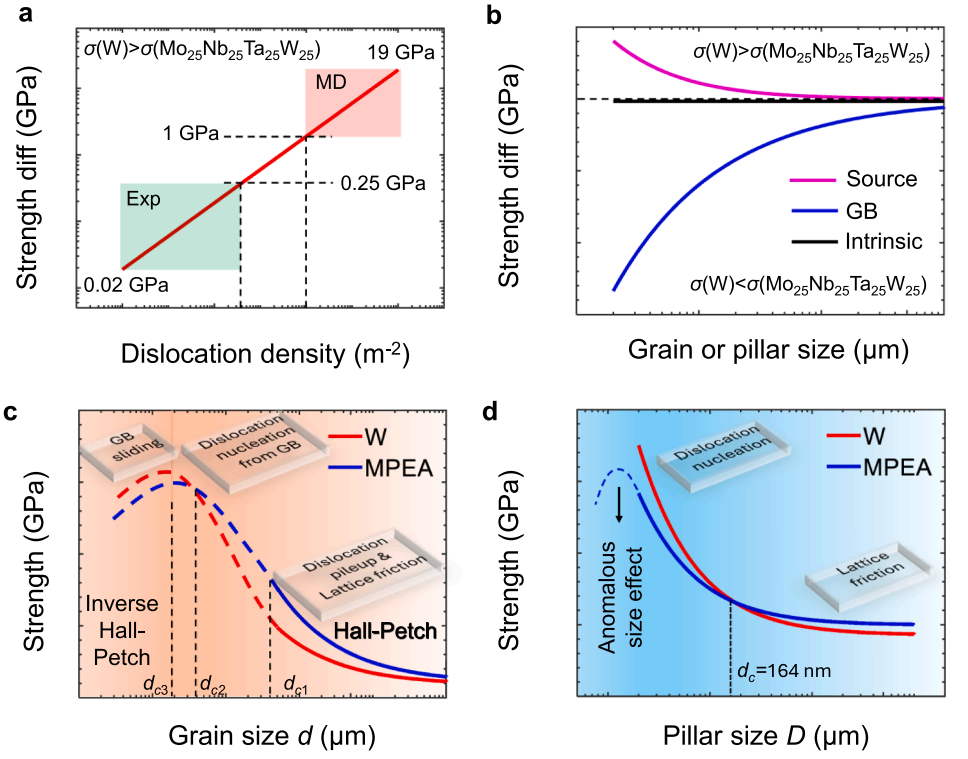

Fig. 15. (a) Forest hardening-induced strength difference between $Mo_{25}Nb_{25}Ta_{25}W_{25}$ and W. The lower green box indicates the region where experiments is applicable, while the upper red box . (b) Strength difference between $Mo_{25}Nb_{25}Ta_{25}W_{25}$ and W due to source nucleation, GB strengthening, and intrinsic strength. Scale and plasticity mechanism-dependent strengths of MPEA and W in (c) polycrystal and (d) single-crystalline nanopillar. The vertical dashed lines indicate the critical grain size at which strengthening mechanism transitions occur.

dislocation-induced solid solution strengthening in MPEAs. Fig. 15(b) shows σ(W)–σ($Mo_{25}Nb_{25}Ta_{25}W_{25}$) with respect to different grain or pillar size. It is seen that only source hardening in Eq. (7) improves W's strength due to its higher shear modulus (G), while GB strengthening significantly enhances $Mo_{25}Nb_{25}Ta_{25}W_{25}$'s strength due to its higher Hall-Petch slope (k). The contribution of intrinsic strength is minor compared to other mechanisms in this small scale.

Next, the transition in the strength superiority in these two systems can be analyzed for the case of polycrystals using Eq. (6). Assuming equivalent dislocation density and grain size, Fig. 15(c) shows that $Mo_{25}Nb_{25}Ta_{25}W_{25}$ (abbreviated as MPEA in the figure) exhibits superior strength compared to W as the grain size decreases as indicated by the solid lines, due to $Mo_{25}Nb_{25}Ta_{25}W_{25}$ outperforming W across all strengthening mechanisms as discussed in Fig. 15(a, b). However, our MD simulations in Figs. 11 and 12 show that W is stronger than $Mo_{25}Nb_{25}Ta_{25}W_{25}$ for very small grains where GB sliding and deformation are the dominating mechanisms, indicative of inverse Hall-Petch behavior in these materials. To reconcile the observed contradiction of strength superiority in both coarse-grain and nano-grain scenarios, Fig. 15(c) presents a conjecture for this transition. Decreasing the grain size below a critical value of d_{c1}, the GB strengthening due to dislocation-GB interaction may be suppressed because GBs become sources and sinks for dislocation (Fig. 15). According to previous work, the critical stress for dislocation nucleation from a GB can be expressed as $\tau \sim Gb/d$ (Chen et al., 2003). This observation is further supported by the data in Figs. 6 and 11, which demonstrate that both the shear modulus and the strength of nano-polycrystalline compression adhere to ROM. Consequently, the shear modulus dominates the strength of materials at this length scale. As a result, the strength difference between W and $Mo_{25}Nb_{25}Ta_{25}W_{25}$ decreases as the grain size decreases. At a critical value of d_{c2}, W exhibits higher strength than $Mo_{25}Nb_{25}Ta_{25}W_{25}$. This trend may continue as the grain size is further reduced to the inverse Hall-Petch regime (below d_{c3}), as captured in our simulation results in Fig. 11.

Furthermore, the strengths derived from single-crystalline micro/nano pillars, as calculated using Eq. (7), are depicted in Fig. 15 (d). This figure highlights the difference in strength between the two systems across various pillar sizes. Notably, there is a critical pillar size $d_c = 164$ nm, below which W is stronger than the $Mo_{25}Nb_{25}Ta_{25}W_{25}$ alloy. This critical size is determined by solving $\sigma_{y,\mathrm{MoNbTaW}} - \sigma_{y,\mathrm{W}} = 0$, where σ_y is calculated using Eq. (7) for both MoNbTaW and W. This can be attributed to the dominance of source hardening over the intrinsic strength difference as the pillar size decreases. Additionally, the strength of $Mo_{25}Nb_{25}Ta_{25}W_{25}$ nanopillars may be compromised by compositional fluctuations (Yan et al., 2022), leading to the anomalous size effect as illustrated by the dashed line in Fig. 15(d). Such effects are absent in pure metals, potentially exaggerating the strength advantage of W over $Mo_{25}Nb_{25}Ta_{25}W_{25}$ at the very small scale. It should be noted that this strength transition is not captured by previous experiments (Zou et al., 2014), likely because the smallest pillar in experiments has the dimeter of 200 nm which is larger than our prediction.

In typical MD, simulations using the high strain rate ($> 10^7$ s^{-1}) and small model size (< 100 nm) usually lead to very high dislocation densities ($> 10^{16}$ m^{-2}). Both high strain rates and high dislocation densities contribute significantly to increasing the strength of materials, as noted in previous studies (El-Awady, 2015; Fan et al., 2021). Fig. 15(a) shows that experimental dislocation densities typically range from 10^{12} to 3×10^{14} m^{-2}, whereas MD simulations exhibit densities in the range of 10^{16} to 10^{18} m^{-2}. These differences in dislocation density lead to varying forest hardening effects in MoNbTaW and W. Specifically, the strength difference ($\sigma_{\mathrm{forest,MoNbTaW}} - \sigma_{\mathrm{forest,W}}$) is approximately 0.02 to 0.25 GPa under experimental conditions, compared to 1 to 19 GPa in MD simulations. Given that the lattice distortion-induced intrinsic strength improvement of MoNbTaW over W is only around 1 GPa, the unphysical forest hardening in MD simulations can lead to W exhibiting higher strength than MoNbTaW. Another factor contributing to the higher strength of W compared to $Mo_{25}Nb_{25}Ta_{25}W_{25}$ in our study is the role of dislocation nucleation as the primary initiation of plasticity in MD simulations. The nanoindentation simulations depicted in Fig. 13 reveal that all free dislocations escape from the bottom, with only a few remaining connected to the top surface. Consequently, hardness is predominantly dictated by dislocation nucleation beneath the indenter. This is in line with recent nanoindentation experiments of MPEAs (Wang and Xu, 2019; Ye et al., 2017; Zhu et al., 2013). Given that dislocation nucleation stress is governed by unstable stacking fault energy (USFE) (Wang et al., 2024b), and USFE follows the rule of mixing (ROM) (Fig. 6), W is expected to have a higher hardness compared to $Mo_{25}Nb_{25}Ta_{25}W_{25}$. This scenario occurs in most existing MD simulations and can explain the discrepancy between experimental results and MD simulations.

In a recent comprehensive review of experimental data on mechanical strength, it was observed that MPEAs do not clearly surpass traditional alloys (George et al., 2020). A key limitation highlighted in this review is the lack of consideration for microstructure engineering in existing MPEA data. This raises an important question: can the mechanical strength of MPEAs consistently exceed that of pure metals in the limiting case? Our study provides a preliminary answer: MPEAs do not surpass the yield strength of their strongest constituent metals at the nanoscale. While MPEAs typically exhibit superior strength in conventional polycrystals—owing to their high intrinsic strength and GB strengthening—this advantage diminishes as the grain size is reduced to the nanoscale. At this scale, the increase in strength observed in both pure metals and MPEAs is accompanied by suppressed dislocation activity. In contrast, deformation is predominantly governed by dislocation nucleation from GBs and GB sliding, with properties such as the shear modulus playing a critical role. In single-crystalline nanopillars or nanoparticles, the maximum strength, defined as the critical shear stress required for homogeneous, barrier-free nucleation of a dislocation loop in a perfect crystal, ranges between $G/30$ and $G/8$, where G represents the shear modulus (Sharma et al., 2018). Given that the shear modulus in MPEAs follows ROM, the strength of single-crystalline MPEAs will not exceed that of their strongest constituent element. This is robustly supported by our nanopillar strength comparisons in Fig. 15(d). Additional experimental evidence supporting our findings is observed in $Al_xCoCrFeNi$ micropillars, where the strength of the micropillars decreases with increasing Al concentration when the pillar size is less than 0.1 μm. Conversely, when the pillar size exceeds 1 μm, the trend is reversed (Jiao et al., 2018). These observations align with our conclusions that solid solution strengthening predominates at larger scales, while at smaller scales, mechanisms such as dislocation nucleation or GB deformation become dominant.

Nevertheless, it is important to note that MPEAs offer several advantages, including enhanced ductility, fatigue resistance, radiation resistance, and resistance to hydrogen embrittlement, all achievable without complex microstructural engineering. Moreover, even when focusing solely on strength, the complex chemical environments within MPEAs create a rugged energy landscape that facilitates sustainable hardening through a progressive synergy of deformation mechanisms, ultimately resulting in a relatively high ultimate strength. In contrast, conventional metals or alloys often face a trade-off between strength and ductility due to conflicting enhancement mechanisms. MPEAs, however, significantly mitigate this contradiction, making them ideal candidates for multifunctional materials suited for demanding environments, such as hydrogen storage and nuclear fusion.

Finally, it is important to acknowledge that incorporating all possible mechanisms and effects, such as screw dislocations, strain rate effect, and temperature effect, in a single study is not feasible. Specifically, screw dislocation strengthening, which has been extensively discussed in previous studies (George et al., 2020; Maresca and Curtin, 2020b; Yin et al., 2021), is not central to this study. Our focus is on demonstrating that the strength superiority of MPEAs is size-dependent, rather than detailing specific strengthening mechanisms like edge or screw dislocations. Furthermore, MPEAs are still evolving materials, and many of their mechanisms are not yet fully understood, such as temperature and strain rate effects. At least, or in the worst case, our findings are applicable under specific conditions: MD simulations conducted at a high strain rate of 300 K or static simulations at 0 K without any strain rate. The temperature and strain-rate dependence of dislocation nucleation stress can be considered in the future (Xiao et al., 2020; Zhu et al., 2008).

6. Conclusion

In this study, the mechanical strength of MoNbTaW MPEAs relative to their constituent metals was investigated through systematic atomistic simulations using both newly developed, highly accurate machine-learning interatomic potentials and established EAM potentials. The results demonstrate that, although the basic properties of MPEAs generally conform to the rule of mixtures and remain bounded by those of the constituent metals, a significant improvement in intrinsic strength is achieved via dislocation strengthening, with MPEAs surpassing pure metals by at least an order of magnitude under certain conditions. However, the mechanical performance of a given MPEA does not uniformly exceed that of its individual elements; rather, its relative strength is dependent on the governing plasticity mechanisms and the observational scale. Notably, MPEAs exhibit superior performance primarily through mechanisms involving solid solution strengthening and dislocation glide, whereas for mechanisms such as dislocation nucleation and grain boundary sliding, certain constituent metals (e.g., W) demonstrate higher strength. These findings underscore the scale- and mechanism-dependent nature of strength superiority in MPEAs, offering valuable insights for microstructural engineering and the design of advanced MPEAs.

CRediT authorship contribution statement

Fei Shuang: Writing – original draft, Writing – review & editing, Validation, Methodology, Data curation, Conceptualization. **Yucheng Ji:** Methodology, Formal analysis. **Luca Laurenti:** Writing – review & editing, Supervision, Methodology, Funding acquisition. **Poulumi Dey:** Writing – review & editing, Supervision, Methodology, Funding acquisition, Conceptualization.

Declaration of competing interest

The authors declare that they have no known competing financial interests or personal relationships that could have appeared to influence the work reported in this paper.

Acknowledgments

This work was sponsored by Nederlandse Organisatie voor WetenschappelijkOnderzoek (The Netherlands Organization for Scientific Research, NWO) domain Science for the use of supercomputer facilities. The authors also acknowledge the use of DelftBlue supercomputer, provided by Delft High Performance Computing Center (https://www.tudelft.nl/dhpc).

Supplementary materials

Supplementary material associated with this article can be found, in the online version, at doi:10.1016/j.ijplas.2025.104308.

Data availability

All simulations were executed using open-source software LAMMPS. All the other codes that support the findings of this study are available from https://github.com/ufsf/Machine-Learning-Potentials/tree/main/MoNbTaW.

References

Alabd Alhafez, I., Ruestes, C.J., Bringa, E.M., Urbassek, H.M., 2019. Nanoindentation into a high-entropy alloy – an atomistic study. J. Alloys Compd. 803, 618–624. https://doi.org/10.1016/J.JALLCOM.2019.06.277.

Alhafez, I.A., Deluigi, O.R., Tramontina, D., Merkert, N., Urbassek, H.M., Bringa, E.M., 2024b. Nanoindentation into a bcc high-entropy HfNbTaTiZr alloy—an atomistic study of the effect of short-range order. Sci. Rep. 14 (1), 1–13. https://doi.org/10.1038/s41598-024-59761-6, 202414.

Bai, Y., Li, Y., Wang, Y.J., Zhang, K., Jiang, Q., Liu, Z., Hu, Z., Wei, B., 2023. Wavy interface enables extra strengthening in an additively manufactured high-entropy alloy with Mortise-Tenon architecture. Int. J. Plast. 170, 103777. https://doi.org/10.1016/J.IJPLAS.2023.103777.

Bartók, A.P., Kondor, R., Csányi, G., 2013. On representing chemical environments. Phys. Rev. B 87, 184115. https://doi.org/10.1103/PhysRevB.87.184115.

Baruffi, C., Maresca, F., Curtin, W.A., 2022. Screw vs. edge dislocation strengthening in body-centered-cubic high entropy alloys and implications for guided alloy design. MRS Commun. 12, 1111–1118. https://doi.org/10.1557/s43579-022-00278-2.

Batatia, I., Benner, P., Chiang, Y., Elena, A.M., Kovács, D.P., Riebesell, J., Advincula, X.R., Asta, M., Avaylon, M., Baldwin, W.J., Berger, F., Bernstein, N., Bhowmik, A., Blau, S.M., Cărare, V., Darby, J.P., De, S., Della Pia, F., Deringer, V.L., Elijošius, R., El-Machachi, Z., Falcioni, F., Fako, E., Ferrari, A.C., Genreith-Schriever, A., George, J., Goodall, R.E.A., Grey, C.P., Grigorev, P., Han, S., Handley, W., Heenen, H.H., Hermansson, K., Holm, C., Jaafar, J., Hofmann, S., Jakob, K.S., Jung, H., Kapil, V., Kaplan, A.D., Karimitari, N., Kermode, J.R., Kroupa, N., Kullgren, J., Kuner, M.C., Kuryla, D., Liepuoniute, G., Margraf, J.T., Magdău, I.-B., Michaelides, A., Moore, J.H., Naik, A.A., Niblett, S.P., Norwood, S.W., O'Neill, N., Ortner, C., Persson, K.A., Reuter, K., Rosen, A.S., Schaaf, L.L., Schran, C., Shi, B.X., Sivonxay, E., Stenczel, T.K., Svahn, V., Sutton, C., Swinburne, T.D., Tilly, J., van der Oord, C., Varga-Umbrich, E., Vegge, T., Vondrák, M., Wang, Y., Witt, W.C., Zills, F., Csányi, G., 2023. A foundation model for atomistic materials chemistry.

Blöchl, P.E., 1994. Projector augmented-wave method. Phys. Rev. B 50, 17953–17979. https://doi.org/10.1103/PhysRevB.50.17953.

Byggmästar, J., Nordlund, K., Djurabekova, F., 2021. Modeling refractory high-entropy alloys with efficient machine-learned interatomic potentials: defects and segregation. Phys. Rev. B 104, 104101. https://doi.org/10.1103/PhysRevB.104.104101.

Cao, P., 2022. Maximum strength and dislocation patterning in multi–principal element alloys. Sci. Adv. 8, 7433. https://doi.org/10.1126/SCIADV.ABQ7433.

Chen, M., Ma, E., Hemker, K.J., Sheng, H., Wang, Y., Cheng, X., 2003. Deformation twinning in nanocrystalline aluminum. Science (1979) 1979 (300), 1275–1277. https://doi.org/10.1126/science.1083727.

Choi, W.-M., Jo, Y.H., Sohn, S.S., Lee, S., Lee, B.-J., 2018. Understanding the physical metallurgy of the CoCrFeMnNi high-entropy alloy: an atomistic simulation study. NPJ Comput. Mater. 4 (1). https://doi.org/10.1038/s41524-017-0060-9.

Cordero, Z.C., Knight, B.E., Schuh, C.A., 2016. Six decades of the Hall–Petch effect – a survey of grain-size strengthening studies on pure metals. Int. Mater. Rev. 61, 495–512. https://doi.org/10.1080/09506608.2016.1191808.

Dai, S.C., Xie, Z.C., Wang, Y.J., 2022. Atomistic interpretation of extra temperature and strain-rate sensitivity of heterogeneous dislocation nucleation in a multi-principal-element alloy. Int. J. Plast. 149, 103155. https://doi.org/10.1016/J.IJPLAS.2021.103155.

Deng, B., Zhong, P., Jun, K., Riebesell, J., Han, K., Bartel, C.J., Ceder, G., 2023. CHGNet as a pretrained universal neural network potential for charge-informed atomistic modelling. Nat. Mach. Intell. 5, 1031–1041. https://doi.org/10.1038/s42256-023-00716-3.

Ding, Q., Zhang, Y., Chen, X., Fu, X., Chen, D., Chen, S., Gu, L., Wei, F., Bei, H., Gao, Y., Wen, M., Li, J., Zhang, Z., Zhu, T., Ritchie, R.O., Yu, Q., 2019. Tuning element distribution, structure and properties by composition in high-entropy alloys. Nature 574, 223–227. https://doi.org/10.1038/s41586-019-1617-1.

Domínguez-Gutiérrez, F.J., Grigorev, P., Naghdi, A., Byggmästar, J., Wei, G.Y., Swinburne, T.D., Papanikolaou, S., Alava, M.J., 2023. Nanoindentation of tungsten: from interatomic potentials to dislocation plasticity mechanisms. Phys. Rev. Mater. 7. https://doi.org/10.1103/PhysRevMaterials.7.043603.

Drautz, R., 2019. Atomic cluster expansion for accurate and transferable interatomic potentials. Phys. Rev. B 99, 014104. https://doi.org/10.1103/PHYSREVB.99.014104.

Duesbery, M.S., Vitek, V., 1998. Plastic anisotropy in b.c.c. transition metals. Acta Mater. 46, 1481–1492. https://doi.org/10.1016/S1359-6454(97)00367-4.

El-Atwani, O., Li, N., Li, M., Devaraj, A., Baldwin, J.K.S., Schneider, M.M., Sobieraj, D., Wróbel, J.S., Nguyen-Manh, D., Maloy, S.A., Martinez, E., 2019. Outstanding radiation resistance of tungsten-based high-entropy alloys. Sci. Adv. 5. https://doi.org/10.1126/sciadv.aav2002 eaav2002.

El-Awady, J.A., 2015. Unravelling the physics of size-dependent dislocation-mediated plasticity. Nat. Commun. 6, 5926. https://doi.org/10.1038/ncomms6926.

Fan, H., Wang, Q., El-Awady, J.A., Raabe, D., Zaiser, M., 2021. Strain rate dependency of dislocation plasticity. Nat. Commun. 12, 1845. https://doi.org/10.1038/s41467-021-21939-1.

Farkas, D., 2021. Deformation behavior of a model high entropy alloy from atomistic simulations. Mater. Sci. Eng. A 812, 141124. https://doi.org/10.1016/J.MSEA.2021.141124.

George, E.P., Curtin, W.A., Tasan, C.C., 2020. High entropy alloys: a focused review of mechanical properties and deformation mechanisms. Acta Mater. 188, 435–474. https://doi.org/10.1016/j.actamat.2019.12.015.

George, E.P., Raabe, D., Ritchie, R.O., 2019. High-entropy alloys. Nat. Rev. Mater. 4, 515–534. https://doi.org/10.1038/s41578-019-0121-4.

Gludovatz, B., Hohenwarter, A., Catoor, D., Chang, E.H., George, E.P., Ritchie, R.O., 2014. A fracture-resistant high-entropy alloy for cryogenic applications. Science (1979) 1979 (345), 1153–1158. https://doi.org/10.1126/science.1254581.

Granberg, F., Nordlund, K., Ullah, M.W., Jin, K., Lu, C., Bei, H., Wang, L.M., Djurabekova, F., Weber, W.J., Zhang, Y., 2016. Mechanism of radiation damage reduction in equiatomic multicomponent single phase alloys. Phys. Rev. Lett. 116, 135504. https://doi.org/10.1103/PhysRevLett.116.135504.

Gupta, A., Jian, W.R., Xu, S., Beyerlein, I.J., Tucker, G.J., 2022. On the deformation behavior of CoCrNi medium entropy alloys: unraveling mechanistic competition. Int. J. Plast. 159, 103442. https://doi.org/10.1016/J.IJPLAS.2022.103442.

Hirel, P., 2015. Atomsk: a tool for manipulating and converting atomic data files. Comput. Phys. Commun. 197, 212–219. https://doi.org/10.1016/j.cpc.2015.07.012.

Hsu, W.-L., Tsai, C.-W., Yeh, A.-C., Yeh, J.-W., 2024. Clarifying the four core effects of high-entropy materials. Nat. Rev. Chem. 8, 471–485. https://doi.org/10.1038/s41570-024-00602-5.

Hua, D., Xia, Q., Wang, W., Zhou, Q., Li, S., Qian, D., Shi, J., Wang, H., 2021. Atomistic insights into the deformation mechanism of a CoCrNi medium entropy alloy under nanoindentation. Int. J. Plast. 142, 102997. https://doi.org/10.1016/j.ijplas.2021.102997.

Huang, G., Zhang, X., Zhang, R., Jian, W.R., Zou, X., Wang, K., Xie, Z., Yao, X., 2024. The shear softening and dislocation glide competition due to the shear-induced short-range order degeneration in CoCrNi medium-entropy alloy. J. Mater. Sci. Technol. 192, 108–122. https://doi.org/10.1016/J.JMST.2023.12.024.

Ikeda, Y, Körmann, F, Lu, W, Gault, B, Ponge, D, Neugebauer, J Su Sohn, S., Kwiatkowski da Silva, A., Ikeda, Y., Körmann, F., Lu, W., Seok Choi, W., Gault, B., Ponge, D., Neugebauer, J., Raabe, S., Sohn, D.S., Kwiatkowski da Silva, A., Raabe, D., Choi, W.S., 2019. Ultrastrong medium-entropy single-phase alloys designed via severe lattice distortion. Adv. Mater. 31, 1807142. https://doi.org/10.1002/ADMA.201807142.

Ji, R., Phan, T., Chen, H., Xiong, L., 2020. Quantifying the dynamics of dislocation kinks in iron and tungsten through atomistic simulations. Int. J. Plast. 128, 102675. https://doi.org/10.1016/j.ijplas.2020.102675.

Jian, W.R., Xie, Z., Xu, S., Su, Y., Yao, X., Beyerlein, I.J., 2020. Effects of lattice distortion and chemical short-range order on the mechanisms of deformation in medium entropy alloy CoCrNi. Acta Mater. 199, 352–369. https://doi.org/10.1016/J.ACTAMAT.2020.08.044.

Jian, W.R., Xu, S., Su, Y., Beyerlein, I.J., 2022. Role of layer thickness and dislocation distribution in confined layer slip in nanolaminated Nb. Int. J. Plast. 152, 103239. https://doi.org/10.1016/J.IJPLAS.2022.103239.

Jiao, Q., Sim, G.-D., Komarasamy, M., Mishra, R.S., Liaw, P.K., El-Awady, J.A., 2018. Thermo-mechanical response of single-phase face-centered-cubic Al $_x$ CoCrFeNi high-entropy alloy microcrystals. Mater. Res. Lett. 6, 300–306. https://doi.org/10.1080/21663831.2018.1446468.

Kang, B., Lee, J., Ryu, H.J., Hong, S.H., 2018. Ultra-high strength WNbMoTaV high-entropy alloys with fine grain structure fabricated by powder metallurgical process. Mater. Sci. Eng. A 712, 616–624. https://doi.org/10.1016/J.MSEA.2017.12.021.

Kresse, G., Furthmüller, J., 1996. Efficiency of ab-initio total energy calculations for metals and semiconductors using a plane-wave basis set. Comput. Mater. Sci. 6, 15–50. https://doi.org/10.1016/0927-0256(96)00008-0.

Laplanche, G., Kostka, A., Reinhart, C., Hunfeld, J., Eggeler, G., George, E.P., 2017. Reasons for the superior mechanical properties of medium-entropy CrCoNi compared to high-entropy CrMnFeCoNi. Acta Mater. 128, 292–303. https://doi.org/10.1016/J.ACTAMAT.2017.02.036.
Lee, C., Maresca, F., Feng, R., Chou, Y., Ungar, T., Widom, M., An, K., Poplawsky, J.D., Chou, Y.-C., Liaw, P.K., Curtin, W.A., 2021. Strength can be controlled by edge dislocations in refractory high-entropy alloys. Nat. Commun. 12, 5474. https://doi.org/10.1038/s41467-021-25807-w.
Lee, S.W., Nix, W.D., 2012. Size dependence of the yield strength of fcc and bcc metallic micropillars with diameters of a few micrometers. Philos. Mag. 92, 1238–1260. https://doi.org/10.1080/14786435.2011.643250.
Lee, T., Qi, J., Gadre, C.A., Huyan, H., Ko, S.T., Zuo, Y., Du, C., Li, J., Aoki, T., Wu, R., Luo, J., Ong, S.P., Pan, X., 2023. Atomic-scale origin of the low grain-boundary resistance in perovskite solid electrolyte Li0.375Sr0.4375Ta0.75Zr0.25O3. Nat. Commun. 14 (1), 1–14. https://doi.org/10.1038/s41467-023-37115-6, 202314.
Li, D., Zhang, Y., 2016. The ultrahigh charpy impact toughness of forged AlxCoCrFeNi high entropy alloys at room and cryogenic temperatures. Intermetallics. (Barking) 70, 24–28. https://doi.org/10.1016/J.INTERMET.2015.11.002.
Li, Q.-J., Sheng, H., Ma, E., 2019a. Strengthening in multi-principal element alloys with local-chemical-order roughened dislocation pathways. Nat. Commun. 10, 3563. https://doi.org/10.1038/s41467-019-11464-7.
Li, W., Tang, J., Wang, Q., Fan, H., 2019b. Molecular dynamics simulations on the mechanical behavior of AlCoCrCu0.5FeNi high-entropy alloy nanopillars. Miner. Met. Mater. Ser. 1271–1280. https://doi.org/10.1007/978-3-030-05861-6_121.
Li, W., Xiang, M., Aitken, Z.H., Chen, S., Xu, Y., Yang, X., Pei, Q., Wang, J., Li, X., Vastola, G., Gao, H., Zhang, Y.-W., 2024. Unraveling the Hall-Petch to inverse Hall-Petch transition in nanocrystalline high entropy alloys under shock loading. Int. J. Plast. 178, 104010. https://doi.org/10.1016/j.ijplas.2024.104010.
Li, W., Xie, D., Li, D., Zhang, Y., Gao, Y., Liaw, P.K., 2021. Mechanical behavior of high-entropy alloys. Prog. Mater. Sci. 118, 100777. https://doi.org/10.1016/J.PMATSCI.2021.100777.
Li, X.-G., Chen, C., Zheng, H., Zuo, Y., Ong, S.P., 2020. Complex strengthening mechanisms in the NbMoTaW multi-principal element alloy. NPJ Comput. Mater. 6, 70. https://doi.org/10.1038/s41524-020-0339-0.
Liu, D., Yu, Q., Kabra, S., Jiang, M., Forna-Kreutzer, P., Zhang, R., Payne, M., Walsh, F., Gludovatz, B., Asta, M., Minor, A.M., George, E.P., Ritchie, R.O., 2022. Exceptional fracture toughness of CrCoNi-based medium- and high-entropy alloys at 20 kelvin. Science (1979) 1979 (378), 978–983. https://doi.org/10.1126/science.abp8070.
Lu, C., Niu, L., Chen, N., Jin, K., Yang, T., Xiu, P., Zhang, Y., Gao, F., Bei, H., Shi, S., He, M.-R., Robertson, I.M., Weber, W.J., Wang, L., 2016. Enhancing radiation tolerance by controlling defect mobility and migration pathways in multicomponent single-phase alloys. Nat. Commun. 7, 13564. https://doi.org/10.1038/ncomms13564.
Luo, H., Lu, W., Fang, X., Ponge, D., Li, Z., Raabe, D., 2018. Beating hydrogen with its own weapon: nano-twin gradients enhance embrittlement resistance of a high-entropy alloy. Mater. Today 21, 1003–1009. https://doi.org/10.1016/j.mattod.2018.07.015.
Luo, H., Sohn, S.S., Lu, W., Li, L., Li, X., Soundararajan, C.K., Krieger, W., Li, Z., Raabe, D., 2020. A strong and ductile medium-entropy alloy resists hydrogen embrittlement and corrosion. Nat. Commun. 11 (1), 1–8. https://doi.org/10.1038/s41467-020-16791-8, 202011.
Lysogorskiy, Y., Bochkarev, A., Mrovec, M., Drautz, R., 2023. Active learning strategies for atomic cluster expansion models. Phys. Rev. Mater. 7, 43801. https://doi.org/10.1103/PhysRevMaterials.7.043801.
Ma, Y., Ma, Y., Wang, Q., Schweidler, S., Botros, M., Fu, T., Hahn, H., Brezesinski, T., Breitung, B., 2021. High-entropy energy materials: challenges and new opportunities. Energy Environ. Sci. 14, 2883–2905. https://doi.org/10.1039/D1EE00505G.
Maresca, F., Curtin, W.A., 2020a. Mechanistic origin of high strength in refractory BCC high entropy alloys up to 1900K. Acta Mater. 182, 235–249. https://doi.org/10.1016/J.ACTAMAT.2019.10.015.
Maresca, F., Curtin, W.A., 2020b. Theory of screw dislocation strengthening in random BCC alloys from dilute to “high-entropy” alloys. Acta Mater. 182, 144–162. https://doi.org/10.1016/J.ACTAMAT.2019.10.007.
Miracle, D.B., Senkov, O.N., 2017. A critical review of high entropy alloys and related concepts. Acta Mater. 122, 448–511. https://doi.org/10.1016/J.ACTAMAT.2016.08.081.
Novikov, I.S., Gubaev, K., Podryabinkin, E.V, Shapeev, A.V, 2021. The MLIP package: moment tensor potentials with MPI and active learning. Mach. Learn. Sci. Technol. 2, 025002. https://doi.org/10.1088/2632-2153/abc9fe.
Okamoto, N.L., Yuge, K., Tanaka, K., Inui, H., George, E.P., 2016. Atomic displacement in the CrMnFeCoNi high-entropy alloy - a scaling factor to predict solid solution strengthening. AIP Adv. 6, 125008. https://doi.org/10.1063/1.4971371/990189.
Perdew, J., Burke, K., Ernzerhof, M., 1996. Generalized gradient approximation made simple. Phys. Rev. Lett. 77, 3865–3868. https://doi.org/10.1103/PhysRevLett.77.3865.
Podryabinkin, E., Garifullin, K., Shapeev, A., Novikov, I., 2023. MLIP-3: active learning on atomic environments with moment tensor potentials. J. Chem. Phys. 159. https://doi.org/10.1063/5.0155887/2908187.
Poul, M., Huber, L., Bitzek, E., Neugebauer, J., 2023. Systematic atomic structure datasets for machine learning potentials: application to defects in magnesium. Phys. Rev. B 107, 104103. https://doi.org/10.1103/PhysRevB.107.104103.
Rao, S.I., Dimiduk, D.M., Tang, M., Parthasarathy, T.A., Uchic, M.D., Woodward, C., 2007. Estimating the strength of single-ended dislocation sources in micron-sized single crystals. Philos. Mag. 87, 4777–4794. https://doi.org/10.1080/14786430701591513.
Romero, R.A., Xu, S., Jian, W.R., Beyerlein, I.J., Ramana, C.V., 2022. Atomistic simulations of the local slip resistances in four refractory multi-principal element alloys. Int. J. Plast. 149. https://doi.org/10.1016/j.ijplas.2021.103157.
Santos-Florez, P.A., Dai, S.-C., Yao, Y., Yanxon, H., Li, L., Wang, Y.-J., Zhu, Q., Yu, X.-X., 2023. Short-range order and its impacts on the BCC MoNbTaW multi-principal element alloy by the machine-learning potential. Acta Mater. 255, 119041. https://doi.org/10.1016/j.actamat.2023.119041.
Senkov, O.N., Wilks, G.B., Miracle, D.B., Chuang, C.P., Liaw, P.K., 2010. Refractory high-entropy alloys. 10.1016/j.intermet.2010.05.014.
Senkov, O.N., Wilks, G.B., Scott, J.M., Miracle, D.B., 2011. Mechanical properties of Nb25Mo25Ta25W25 and V20Nb20Mo20Ta20W20 refractory high entropy alloys. Intermetallics. (Barking) 19, 698–706. https://doi.org/10.1016/J.INTERMET.2011.01.004.
Shapeev, A.V., 2016. Moment tensor potentials: a class of systematically improvable interatomic potentials. 10.1137/15M1054183 14, 1153–1173.
Sharma, A., Hickman, J., Gazit, N., Rabkin, E., Mishin, Y., 2018. Nickel nanoparticles set a new record of strength. Nat. Commun. 9, 4102. https://doi.org/10.1038/s41467-018-06575-6.
Sheriff, K., Cao, Y., Smidt, T., Freitas, R., 2024. Quantifying chemical short-range order in metallic alloys. Proc. Natl. Acad. Sci. U. S.A. 121, e2322962121. https://doi.org/10.1073/PNAS.2322962121.
Shuang, F., Laurenti, L., Dey, P., 2025. Standard deviation in maximum restoring force controls the intrinsic strength of face-centered cubic multi-principal element alloys. Acta Mater. 282, 120508. https://doi.org/10.1016/j.actamat.2024.120508.
Shuang, S., Lu, S., Zhang, B., Bao, C., Kan, Q., Kang, G., Zhang, X., 2021. Effects of high entropy and twin boundary on the nanoindentation of CoCrNiFeMn high-entropy alloy: a molecular dynamics study. Comput. Mater. Sci. 195, 110495. https://doi.org/10.1016/J.COMMATSCI.2021.110495.
Stukowski, A., 2010. Visualization and analysis of atomistic simulation data with OVITO–the open visualization tool. Model. Simul. Mat. Sci. Eng. 18, 015012. https://doi.org/10.1088/0965-0393/18/1/015012.
Sun, Y., Dai, S., 2021. High-entropy materials for catalysis: a new frontier. Sci. Adv. 7. https://doi.org/10.1126/SCIADV.ABG1600/ASSET/0B8BA449-7251-4A98-A8C7-157A2A1571C6/ASSETS/GRAPHIC/ABG1600-F6.JPEG.
Suzuki, T., Kamimura, Y., Kirchner, H.O.K., 1999. Plastic homology of bcc metals. Philos. Mag. A 79, 1629–1642. https://doi.org/10.1080/01418619908210383.
Tan, A.M.Z., Li, Z., Zhao, Y., Ramamurty, U., Gao, H., 2024. Modeling the improved hydrogen embrittlement tolerance of twin boundaries in face-centered cubic complex concentrated alloys. J. Mech. Phys. Solids 105657. https://doi.org/10.1016/j.jmps.2024.105657.
Tandoc, C., Hu, Y.-J., Qi, L., Liaw, P.K., 2023. Mining of lattice distortion, strength, and intrinsic ductility of refractory high entropy alloys. NPJ Comput. Mater. 9, 53. https://doi.org/10.1038/s41524-023-00993-x.

Thompson, A.P., Aktulga, H.M., Berger, R., Bolintineanu, D.S., Brown, W.M., Crozier, P.S., in 't Veld, P.J., Kohlmeyer, A., Moore, S.G., Nguyen, T.D., Shan, R., Stevens, M.J., Tranchida, J., Trott, C., Plimpton, S.J., 2022. LAMMPS - a flexible simulation tool for particle-based materials modeling at the atomic, meso, and continuum scales. Comput. Phys. Commun. 271, 108171. https://doi.org/10.1016/j.cpc.2021.108171.

Utt, D., Lee, S., Xing, Y., Jeong, H., Stukowski, A., Oh, S.H., Dehm, G., Albe, K., 2022. The origin of jerky dislocation motion in high-entropy alloys. Nat. Commun. 13, 4777. https://doi.org/10.1038/s41467-022-32134-1.

Varvenne, C., Luque, A., Curtin, W.A., 2016a. Theory of strengthening in fcc high entropy alloys. Acta Mater. 118, 164–176. https://doi.org/10.1016/J.ACTAMAT.2016.07.040.

Varvenne, C., Luque, A., Nöhring, W.G., Curtin, W.A., 2016b. Average-atom interatomic potential for random alloys. Phys. Rev. B 93, 104201. https://doi.org/10.1103/PhysRevB.93.104201.

Wang, H., He, Q., Gao, X., Shang, Y., Zhu, W., Zhao, W., Chen, Z., Gong, H., Yang, Y., 2024a. Multifunctional high entropy alloys enabled by severe lattice distortion. Adv. Mater. 36, 2305453. https://doi.org/10.1002/ADMA.202305453.

Wang, L., Cao, Y., Zhao, Y., 2024b. Lattice distortion promotes incipient plasticity in multiprincipal element alloys. Nano Lett. 24, 9004–9010. https://doi.org/10.1021/acs.nanolett.4c02086.

Wang, S.P., Xu, J., 2019. Incipient plasticity and activation volume of dislocation nucleation for TiZrNbTaMo high-entropy alloys characterized by nanoindentation. J. Mater. Sci. Technol. 35, 812–816. https://doi.org/10.1016/J.JMST.2018.11.014.

Wang, T., Li, J., Wang, M., Li, C., Su, Y., Xu, S., Li, X.-G., 2024c. Unraveling dislocation-based strengthening in refractory multi-principal element alloys. NPJ Comput. Mater. 10, 143. https://doi.org/10.1038/s41524-024-01330-6.

Wang, V., Xu, N., Liu, J.C., Tang, G., Geng, W.T., 2021. VASPKIT: a user-friendly interface facilitating high-throughput computing and analysis using VASP code. Comput. Phys. Commun. 267, 108033. https://doi.org/10.1016/J.CPC.2021.108033.

Wu, Z., Bei, H., Otto, F., Pharr, G.M., George, E.P., 2014a. Recovery, recrystallization, grain growth and phase stability of a family of FCC-structured multi-component equiatomic solid solution alloys. Intermetallics. (Barking) 46, 131–140. https://doi.org/10.1016/j.intermet.2013.10.024.

Wu, Z., Bei, H., Pharr, G.M., George, E.P., 2014b. Temperature dependence of the mechanical properties of equiatomic solid solution alloys with face-centered cubic crystal structures. Acta Mater. 81, 428–441. https://doi.org/10.1016/J.ACTAMAT.2014.08.026.

Xiao, J., Wu, N., Ojo, O., Deng, C., 2020. Dislocation nucleation in CoNiCrFeMn high entropy alloy. Materialia (Oxf) 12, 100749. https://doi.org/10.1016/J.MTLA.2020.100749.

Xie, Z., Jian, W.R., Xu, S., Beyerlein, I.J., Zhang, X., Yao, X., Zhang, R., 2022. Phase transition in medium entropy alloy CoCrNi under quasi-isentropic compression. Int. J. Plast. 157. https://doi.org/10.1016/j.ijplas.2022.103389.

Xiong, L., Xu, S., McDowell, D.L., Chen, Y., 2015. Concurrent atomistic–continuum simulations of dislocation–void interactions in fcc crystals. Int. J. Plast. 65, 33–42. https://doi.org/10.1016/j.ijplas.2014.08.002.

Xu, S., Jian, W.R., Su, Y., Beyerlein, I.J., 2022. Line-length-dependent dislocation glide in refractory multi-principal element alloys. Appl. Phys. Lett. 120, 61901. https://doi.org/10.1063/5.0080849/2833058.

Xu, X., Zhang, X., Bitzek, E., Schmauder, S., Grabowski, B., 2024. Origin of the yield stress anomaly in L1 intermetallics unveiled with physically informed machine-learning potentials. Acta Mater. 281, 120423. https://doi.org/10.1016/j.actamat.2024.120423.

Yan, J., Yin, S., Asta, M., Ritchie, R.O., Ding, J., Yu, Q., 2022. Anomalous size effect on yield strength enabled by compositional heterogeneity in high-entropy alloy nanoparticles. Nat. Commun. 13, 2789. https://doi.org/10.1038/s41467-022-30524-z.

Ye, Y.X., Lu, Z.P., Nieh, T.G., 2017. Dislocation nucleation during nanoindentation in a body-centered cubic TiZrHfNb high-entropy alloy. Scr. Mater. 130, 64–68. https://doi.org/10.1016/J.SCRIPTAMAT.2016.11.019.

Yin, S., Zuo, Y., Abu-Odeh, A., Zheng, H., Li, X.-G., Ding, J., Ong, S.P., Asta, M., Ritchie, R.O., 2021. Atomistic simulations of dislocation mobility in refractory high-entropy alloys and the effect of chemical short-range order. Nat. Commun. 12, 4873. https://doi.org/10.1038/s41467-021-25134-0.

Zhang, L., Xiang, Y., Han, J., Srolovitz, D.J., 2019. The effect of randomness on the strength of high-entropy alloys. Acta Mater. 166, 424–434. https://doi.org/10.1016/j.actamat.2018.12.032.

Zhang, Q., Niu, R., Liu, Y., Jiang, J., Xu, F., Zhang, X., Cairney, J.M., An, X., Liao, X., Gao, H., Li, X., 2023a. Room-temperature super-elongation in high-entropy alloy nanopillars. Nat. Commun. 14, 7469. https://doi.org/10.1038/s41467-023-42894-z.

Zhang, Z., Cai, W., Feng, Y., Duan, G., Wang, Jing, Wang, Jun, Yang, R., Xiao, P., Ke, F., Lu, C., 2023b. Dislocation reactions dominated pop-in events in nanoindentation of Ni-based single crystal superalloys. Mater. Charact. 200, 112883. https://doi.org/10.1016/j.matchar.2023.112883.

Zhao, S., Osetsky, Y., Stocks, G.M., Zhang, Y., 2019. Local-environment dependence of stacking fault energies in concentrated solid-solution alloys. NPJ Comput. Mater. 5, 13. https://doi.org/10.1038/s41524-019-0150-y.

Zhou, X.W., Johnson, R.A., Wadley, H.N.G., 2004. Misfit-energy-increasing dislocations in vapor-deposited CoFe/NiFe multilayers. Phys. Rev. B 69, 144113. https://doi.org/10.1103/PhysRevB.69.144113.

Zhou, Y., Srinivasan, P., Körmann, F., Grabowski, B., Smith, R., Goddard, P., Duff, A.I., 2022. Thermodynamics up to the melting point in a TaVCrW high entropy alloy: systematic ab initio study aided by machine learning potentials. Phys. Rev. B 105. https://doi.org/10.1103/PHYSREVB.105.214302/FIGURES/9/MEDIUM.

Zhu, C., Lu, Z.P., Nieh, T.G., 2013. Incipient plasticity and dislocation nucleation of FeCoCrNiMn high-entropy alloy. Acta Mater. 61, 2993–3001. https://doi.org/10.1016/J.ACTAMAT.2013.01.059.

Zhu, J., Xie, J., Wang, J., Xia, X., Lin, Z., Qian, G., Zhao, A., 2024. Low-cycle and dwell fatigue properties for a near alpha titanium alloy Ti–6Al–3Nb–2Zr–1Mo. J. Mater. Res. Technol. 29, 2204–2215. https://doi.org/10.1016/J.JMRT.2024.01.287.

Zhu, T., Li, J., Samanta, A., Leach, A., Gall, K., 2008. Temperature and strain-rate dependence of surface dislocation nucleation. 10.1103/PhysRevLett.100.025502.

Zou, Y., Ma, H., Spolenak, R., 2015. Ultrastrong ductile and stable high-entropy alloys at small scales. Nat. Commun. 6, 7748. https://doi.org/10.1038/ncomms8748.

Zou, Y., Maiti, S., Steurer, W., Spolenak, R., 2014. Size-dependent plasticity in an Nb25Mo25Ta25W25 refractory high-entropy alloy. Acta Mater. 65, 85–97. https://doi.org/10.1016/j.actamat.2013.11.049.

Zuo, Y., Chen, C., Li, X., Deng, Z., Chen, Y., Behler, J., Csányi, G., Shapeev, A.V., Thompson, A.P., Wood, M.A., Ong, S.P., 2020. Performance and cost assessment of machine learning interatomic potentials. J. Phys. Chem. A 124, 731–745. https://doi.org/10.1021/acs.jpca.9b08723.